Fusion Engineering and Design 202 (2024) 114329

Contents lists available at ScienceDirect

Fusion Engineering and Design

journal homepage: www.elsevier.com/locate/fusengdes

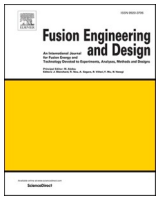

The integrated engineering design concept of the upper limiter within the EU-DEMO LIMITER system

M.L. Richiusa [a,b,*], A. Cardella [c], A. Čufar [d], A. Froio [c,e], P. Haghdoust [g], P. Ireland [a], I. Maione [c,f], I. Pagani [g], G. Pautasso [h], A. Martin Ramos [i], G.A. Spagnuolo [j], F. Vigano [g], Z. Vizvary [b]

[a] Department of Engineering Science, Oxford Thermofluids Institute, University of Oxford, Oxford, OX2 0ES, UK
[b] UKAEA, Culham Campus, Abingdon, Oxfordshire, OX14 3DB, UK
[c] Consultant, 85598 Baldham, Germany
[d] Reactor Physics Department, Jožef Stefan Institute, Jamova cesta 39, SI-1000 Ljubljana, Slovenia
[e] NEMO Group, Dipartimento Energia, Politecnico di Torino, 10129 Turin, Italy
[f] Karlsruhe Institute of Technology, Karlsruhe, Germany
[g] LTCalcoli srl, Via Bergamo 60, 23807 Merate (LC), Italy
[h] Max Planck Institute for Plasma Physics, Boltzmannstrasse 2, 85748 Garching, Germany
[i] Empresarios Agrupados International, 28015 Madrid, Spain
[j] EUROfusion – Programme Management Unit, Boltzmannstrasse 2, 85748 Garching, Germany

ARTICLE INFO

Keywords:
EU-DEMO upper limiter
Integrated design
EM
Neutronics
Thermal-hydraulics
Structural integrity

ABSTRACT

The EU-DEMO first wall protection relies on a system of limiters. Although they are primarily designed for facing the energy released by a limited plasma during transients, their design should safely withstand a combination of loads relevant for in-vessel components (IVCs) during steady-state operation. They are not meant to breed tritium, nor to provide plasma stability. However, sitting in place of blanket portions, they should ensure an adequate shielding function to vacuum vessel and magnets while withstanding both their dead weight and the electro-mechanical loads arising from the interaction between current induced in the conductive structure and magnetic field. During plasma disruptions they will be subjected to halo currents flowing from/to the plasma and the grounded structures, whose effects must be added to the eddy current ones. Disruption-induced electro-mechanical loads are hence IVC design-driving, despite the uncertainties in both eddy and halo currents' magnitude and distribution, which depend on IVC design, electrical connectivity, plasma temperature and halo width.

The integrated design of the limiter is made of two actively water-cooled sub-components: the Plasma-Facing Wall (PFW) directly exposed to the plasma, and the Shielding Block (SB) devoted to hold the PFW while providing neutronic shielding. The PFW design is driven by disruptive heat loads. Disruption-induced electro-magnetic loads are instead SB design drivers, meaning that the design details (i.e. geometry, electrical connections, attachments) affect the loads acting on it, which, in turn, are affected by the mechanical response of the structure.

The present paper describes the design workflow and assessment of the Upper Limiter (UL), resulting from a close and iterative synergy among different fields. Built on static-structural and energy balance hand calculations based on, respectively, preliminary electro-magnetic and neutronic loads, the UL integrated design performance has then been verified against electro-magnetic, neutronic, thermal-hydraulic and structural assessment under the above-mentioned load combination. The outcome will be taken as reference for future limiter engineering designs.

* Corresponding author.
E-mail address: lorena.richiusa@ukaea.uk (M.L. Richiusa).

https://doi.org/10.1016/j.fusengdes.2024.114329
Received 13 October 2023; Received in revised form 19 January 2024; Accepted 7 March 2024
Available online 16 March 2024

1. Introduction

Normal and off-normal plasma transients are certainly challenging for in-vessel components (IVCs), as they are responsible for releasing energy into the component when hit by the plasma in its limited configuration. Furthermore, off-normal transients induce electro–mechanical loads due to the interaction between currents induced in the conductive structure and $\vec{B}$. Although the EU-DEMO first wall (FW) protection strategy against plasma-wall contacts foresees protruding limiters dealing with plasma energy release, their design should safely withstand and minimize the impacts of these loads onto the structure. This means that although limiters are primarily designed for facing plasma energy releases, their integrated design should safely withstand dead weight and electro-magnetic (EM) loads, while ensuring adequate neutronic shielding to vacuum vessel (VV) and magnets. Limiters are installed in place of the blanket, directly attached to the VV. As a general consideration, they should preferably be located near openings which enable them to be installed and easily replaced when needed. Where physics suggests a different location on the wall, an engineering design solution supported by realistic handling strategies should be put in place.

This paper mainly focuses on the description of the Upper Limiter (UL) design concept, and it is organized as follows. After a brief overview of the EU-DEMO LIMITER (LIM) system, the integrated design concept of the UL is presented. The rationale behind the design choices of every UL sub-system is highlighted, and then supported by an extensive assessment workflow, based on neutronics and thermal-hydraulics evaluations (respectively, in §5.1 and §5.2), EM studies (§5.3) and structural assessment (§5.4).

2. The LIM system baseline

Fig. 1 shows a top view of the LIM system embedded within the DEMO tokamak, whose toroidal symmetry has now a 45° cyclic periodicity. The physical assumptions defining the LIM System as FW protection strategy are explained in [1].

The general architecture of the LIM System foresees two limiter sub-systems according to their specific functions. The first sub-system is designed to withstand normal operation plasma transients, e.g. ramp-up/down phases, and consists of four Outboard Midplane Limiters (OMLs), located every 90° in the main equatorial outboard ports. The second sub-system is designed to withstand off-normal transients caused by disruptive events and consists of: eight Upper Limiters (ULs) for Upward Vertical Displacement Events (UVDE), located every 45° below the upper port; four Outboard Lower Limiters (OLLs) for Downward VDEs, located below the four OMLs; four additional Inboard Midplane Limiters (IMLs), located every 90°, or, alternatively, a reinforced inboard breeding blanket armour, are also currently considered for inboard wall protection purposes. The limiters devoted to protecting the FW against off-normal events are also referred to as "sacrificial" as their armour can be damaged under up to GJ of energy released in milliseconds, provided that the integrity of the cooling system is maintained.

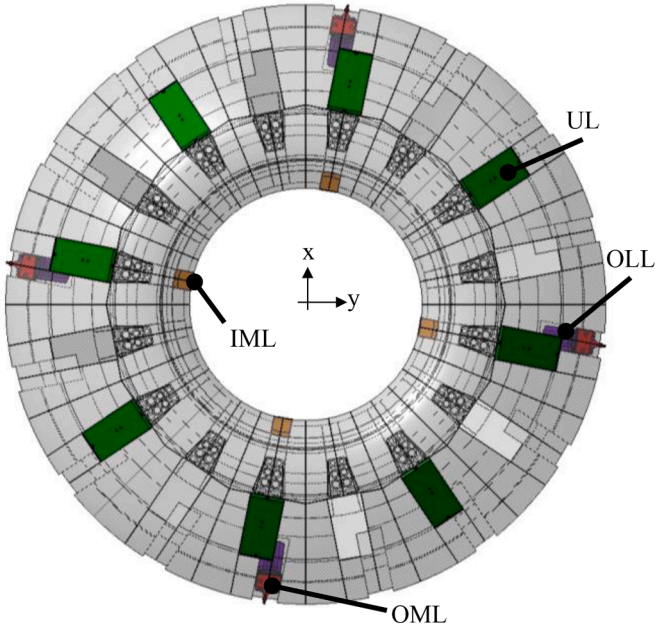

Fig. 1. Top view of the LIM System architecture embedded within the 360° DEMO tokamak.

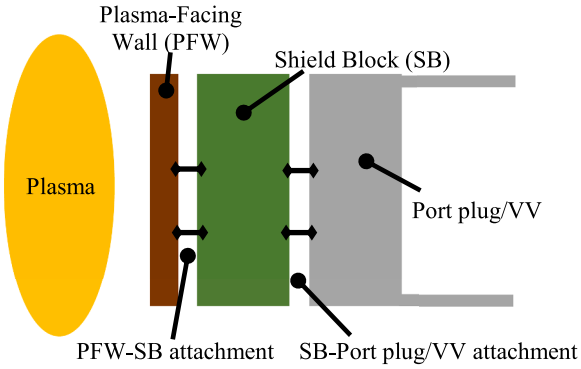

Fig. 2. LIM unit sketch.

The general structure of a limiter unit foresees three different parts highlighted in Fig. 2:

- Plasma-Facing Wall (PFW), directly facing the plasma energy release and made of W;
- Shielding Block (SB), which holds the PFW and shields all the components behind it from the neutronic flux. This will be made of EUROFER97 steel;
- Cooling pipes running through both the PFW and the SB, as they are actively cooled.

3. Cooling system temperature level requirements

For reducing the numbers of cooling systems feeding the DEMO IVCs, and because of some important similar requirements, it is advantageous to use similar coolant pressure and temperature inlet values for limiter and divertor systems.

- For the SB, the working temperature of EUROFER should ensure sufficient ductile behaviour under neutron irradiation during both operation and maintenance. Therefore, Pressurized Water Reactors (PWR) cooling conditions help EUROFER work within good safety margins against embrittlement, over a temperature range where the Ductile-To-Brittle Transition (DBTT) is mainly independent from damage (dpa). This also makes the extension of the SB lifetime and its re-use after annealing possible.

Table 1
Temperature and pressure inlet values of the PFW and SB cooling systems.

	ΔT_{inlet} [°C]	ΔP_{inlet} [MPa]	T_{inlet_UL} [°C]	P_{inlet_UL} [MPa]	$\langle v \rangle_{inlet\_UL}$ [m s^{-1}]
PFW	70–140	5.0–6.5	130	5	12(§4.2)
SB	280–295	14.0–16.0	295	15.5	3(§4.2)

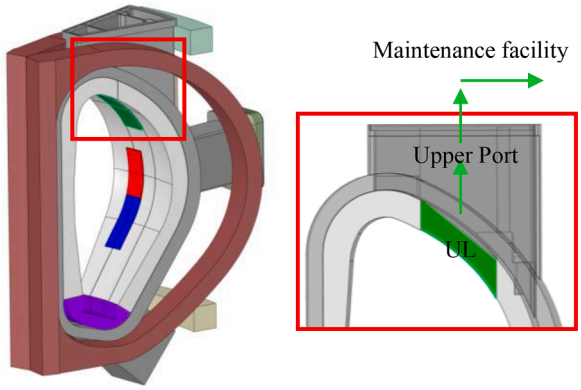

Fig. 3. UL position within the 22.5° EU-DEMO sector.

- For the PFW, due to the most stringent normal operation conditions faced by the divertor, the PFW inlet parameters are assumed within the ΔT_{inlet} and ΔP_{inlet} ranges highlighted in Table 1, which also reports the inlet parameters assumed for the UL first design point.
- Both systems are non-tritium breeding IVCs subjected to neutron flux, adopt a refractory armor coping with the plasma heat loads, and are subjected to high heat flux, different in intensity and duration.

4. The integrated design concept of the UL

The UL is a port-based limiter, located within the upper port projection as highlighted in Fig. 3, through which it is remotely handled separately from any other IVCs. The UL is directly attached to the upper port plug, with which it is assembled before being installed in-vessel. Any removal of the UL also occurs jointly with the port plug by means of a set of single axis translations that lift and transport the UL-port plug assembly to the maintenance facility, where the dismantling between port plug and UL occurs, as well as between UL PFW and SB.

The UL is mainly devoted to withstanding UVDEs, especially the ones bringing the fully energetic plasma to drift upwards until it touches the wall.

The integrated design of the UL is shown in Fig. 4. The rationale of the design choices will be explained separately for each limiter unit's sub-system, i.e. PFW and SB, in §4.1 and §4.2, respectively.

4.1. PFW design

The disruptive heat loads are the main design drivers of the PFW, since this is directly exposed to plasma thermal loads. In particular, the PFW should be designed to withstand the plasma energy release during the VDE plasma thermal quench (TQ). Although its final configuration requires R&D studies on different technologies like the ones described in [2], a provisional PFW layout is here implemented by using the W monoblock configuration already adopted by the DEMO divertor [3].

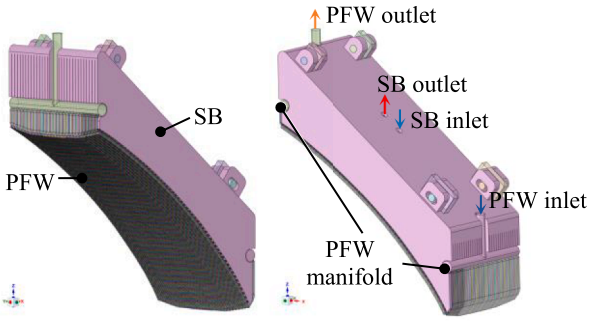

Fig. 4. Overview of the integrated engineering design of the UL.

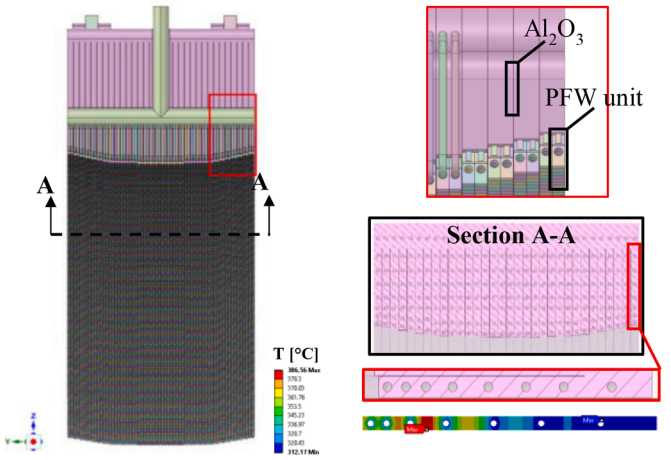

Fig. 5. Particular of the PFW–SB interface (top red box) and the SB slicing (bottom black box, Section A-A).

Since it is likely that the first layers of the W armor will experience localized melting following disruptive events, there is the need to estimate the minimum safest armor thickness to protect the cooling system beneath it. This estimate is continued from a previous work referenced in [4], which sets the thickness of the W armor to 20 mm when the bulk W monoblock configuration is analysed under a thermal transient typical of UVDE foreseen for DEMO.

The zero estimate of the PFW hydraulic parameters is based on energy conservation principle. The total integrated power deposited by both neutrons (see Table 4 in §6) and ionized particles on the PFW is 5.4 MW. By assuming that this power is uniformly deposited into the 64 units, this results in 0.084 MW per PFW unit (Fig. 5). The mass flow rate required by every PFW unit to remove this heat is calculated as $\dot{m} = \rho v A = 1.3\,kg\,s^{-1}$, by imposing a maximum fluid velocity of 12 m s^{-1} on a given geometry [3]. The heat transfer coefficient (HTC) is derived from the dimensionless numbers reported in Table 1, using the Dittus–Boelter correlation [5]. Having imposed the cross-section area of the pipes and the fluid velocity, it follows that $T_{outlet} = 146\,°C$ and $\Delta T = T_{outlet} - T_{inlet} = 16\,°C$. The study on PFW armor thickness estimate in [4] is based on these calculated parameters.

4.2. EUROFER SB design

During the VDE current quench (CQ) following the TQ, the plasma current decay induces toroidal and poloidal currents in conducting structures, and halo currents flowing between the plasma and the grounded structures as the plasma shrinks while cooling down. The magnitude and distribution of these currents depend on VV and IVC design, electrical connectivity, and plasma conditions, which are difficult to quantify. Disruption-induced EM loads are IVCs design drivers, to be added to the normal operation load combination due to gravity, internal and external pressure, neutronic heating, temperature gradients, and earthquakes, which produce a complex loading pattern. The EM loads are, in turn, also affected by the design features and the mechanical response of the components. Therefore, the design of the limiter SB is mainly driven by EM loads acting on it during disruptive events, when the time variation of $\vec{B}_\theta$ induces eddy currents in the conductive structures trying to oppose its variation. The interaction between these currents and the static $\vec{B}_\phi$ can generate large EM loads. As the magnitude of the Lorentz forces $(\vec{I} \times \vec{B}_\phi)$ can be reduced by minimizing the eddy current radial paths, similarly to [6] the conceptual design of the ferromagnetic SB consists of 32 poloidally–oriented 50 mm–thick EUROFER97 plates separated by 1 mm-thick electrical insulator (like Al_2O_3, see Fig. 5), to keep each plate electrically insulated while

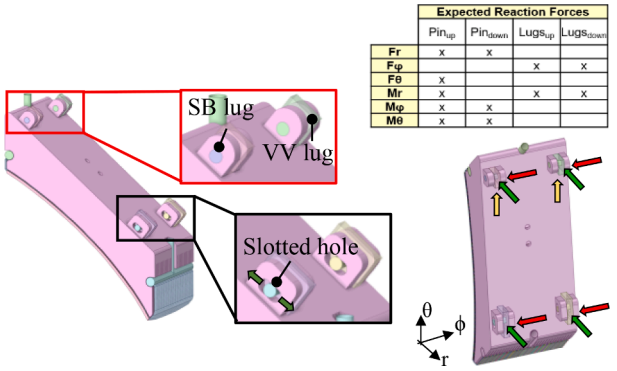

Fig. 6. SB-VV attachment system. Lhs: particular of the SB upper pin connections, and SB lower slotted hole pin connections; rhs: locations of the expected reaction forces.

avoiding accidental contact between adjacent plates. Each Al_2O_3 layer extends radially for almost the entire depth of the limiter. At the back, the plates are HIPed together to create a stiffer back–supporting structure. The attachment system to the VV is provided at the back of the supporting structure. Every plate is actively water-cooled by serpentine tubes running in parallel and having common inlet and outlet manifolds, which are embedded within the SB.

Every plate supports two PFW monoblock units (Fig. 5), fastened to each plate by joints whose design is not part of this study, and for which the same solution adopted for the divertor system is temporarily considered [3] for the reasons already explained in §4.1.

The SB-VV attachment system is required to (a) hold the limiter against its dead weight; (b) reliably react against EM forces and moments; (c) allow the limiter to thermally expand; (d) be easily assembled and dismantled in the maintenance facility.

As a first approximation, the sizing of the fixations is based on previous estimates of Lorentz and ferromagnetic loads acting on the simplified UL geometry during UVDE in [7].

The proposed attachment system is built on pin-lug-plug connections at the four corners of the SB back-supporting structure (Fig. 6). A single attachment point foresees a pin reacting to loads that act perpendicularly to its axis, supported by lugs with circular holes through which the pin is inserted. The distance between each connection point is maximized for minimizing the reaction force magnitude acting on pins. The bottom SB lugs foresee a slotted hole allowing the limiter to freely expand poloidally without additional constraints. Indeed, considering that the limiter would go from 40 °C to its averaged operating temperature 350 °C (from Fig. 5), the poloidal thermal expansion is larger than the toroidal one ($L_{\theta,0} \approx 3.5$ m, $L_{\varphi,0} \approx 1.48$ m, $\alpha_{EU97} = 1.175E-5\ °C^{-1}$) and, hence, $\Delta L_\varphi << \Delta L_\theta$.

Sitting in place of the breeding blanket, the limiter SB should provide enough shielding to VV (by limiting the displacement per atom - dpa), and magnets (by limiting the deposited energy) [8]. Hence, the SB internals design is driven by neutronic considerations. The SB is made of a mixture of EUROFER (92.85 %), Al_2O_3 (1.87 %), and water (5.28 %).

The radial distribution of the cooling tubes is calculated by assuming that the power deposited into the SB under neutronic irradiation is $P_{SB} = 4.5$ MW (see Table 4 in §6) and is uniformly distributed over 32 plates. Imposing an inlet and outlet temperatures of, respectively, $T_{inlet} = 295$ °C and $T_{outlet} = 328$ °C, the calculated mass flow rate needed for cooling down the SB is ≈ 23 kg s^{-1}. For a single plate, it follows $\dot{m} = 0.7$ kg m^{-2} s^{-1}. By choosing the internal diameter of the cooling tubes equal to 0.02 m, the calculated average coolant velocity is equal to $v = 3$ m s^{-1}. The dimensionless numbers in Table 2 give an estimated average of the HTC at the pipe's inner wall, with an average bulk temperature equal to $T_{ave} = 0.5(T_{inlet}+T_{outlet}) = 312$ °C.

These conditions are used for a 2D model representative of one plate's cross-section (Fig. 5). The cooldown is implemented as convective boundary condition (BC) at the pipe's inner wall, by considering the above–calculated constant values of HTC and T_{ave}. Tubes are radially spaced for keeping the EUROFER operational temperature within the interval 300–550 °C.

Table 2
PFW and SB hydraulic cooling system parameters.

	Re	Pr	Nu	HTC [$Wm^{-2}K^{-1}$]
PFW	6.4E + 05	9.0E-01	1.1E + 03	5.7E+04
SB	5.6E + 05	9.0E-01	8.7E + 02	2.3E+04

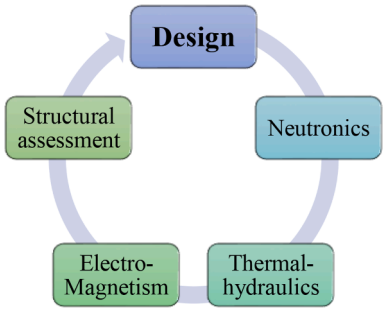

Fig. 7. UL engineering design assessment workflow.

5. Assessment workflow

The UL engineering design is here supported by an assessment workflow, which aims at verifying that the design choices are robust enough for enabling the UL to perform well under the load combination it is designed for. This section describes the main steps of the assessment workflow sketched in Fig. 7, which starts from neutronic evaluations for studying the shielding performances, as well as for providing the volumetric power deposition input to thermal-hydraulic analyses. These analyses estimate the temperature distribution of the 3D domain and verify that the requirements on working temperature are fulfilled. The EM assessment aims at calculating the EM loads under operating conditions and accidental scenarios. These outputs are fed into the structural assessment, which finally highlights any week point in the structural design under the foreseen load combinations.

5.1. Neutronics

The models for the neutronic simulations are created by converting sufficiently simplified CAD geometries into MCNP models using SuperMC [9], while MCNP5 v1.60 [10] with JEFF3.3 [11] nuclear data are used for the simulations. The analyses are performed in two stages.

In the first stage a simplified model is used to perform basic analyses such as total nuclear heating in components and radial dependence of the nuclear heating in the SB. These analyses are crucial for the development of the cooling solution in §4.1 and §4.2. The model is shown in Fig. 8 and consists of 3 layered PFW and a single homogenized layer representing a SB. Two geometrically different options are considered for SB, namely a "box design", where the SB is a EUROFER box filled with water, and a "sliced design", a design made of EUROFER plates cooled with water tubes. For the "sliced design", two SB cooling options characterized by different water temperature and density are considered. This represents the two cases where the SB would either have the same temperature as the PFWs ("plate design", with one single cooling system shared between PFW and SB) or different temperature ("alternative plate design", with two separate cooling systems between PFW and SB). These different choices are simulated using different homogenized material mixes for the SB. The material composition of the three PFW layers is the same in all three cases. The assumed material

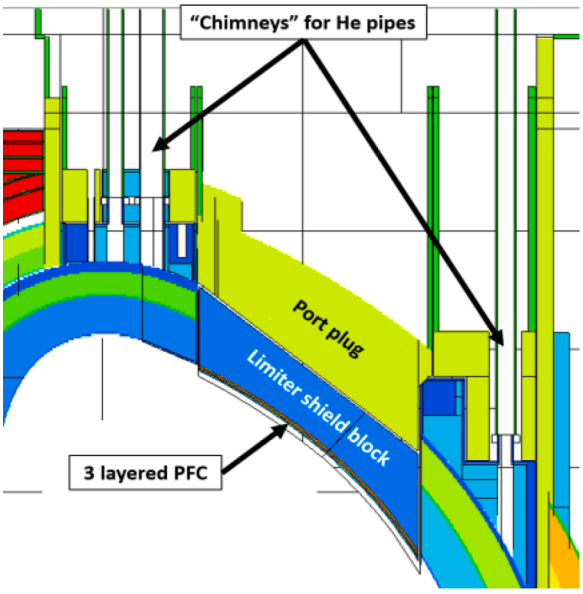

Fig. 8. Simple MCNP model of the upper limiter for HCPB TBB case.

Table 3
Material composition (in%volume) for different layers of the UL simple neutronics model.

	Box design	Plate design	Alter plate design
PFW-1	W		
PFW-2 – tube layer	W (39.5 %), CuCrZr (17.0 %), oxygen free Cu (13.5 %), water (30 %)		
PFW-3 – W bottom layer	EUROFER (39.5 %), W (21.0 %), void (39.5 %)		
SB	EUROFER (53 %), water (47 %, at 0.92 g/cm^3)	EUROFER (87.5 %), water (7.4 % at 0.92 g/cm^3), void (5.1 %)	EUROFER (87.5 %), water (7.4 % at 0.7 g/cm^3), void (5.1 %)

Table 4
Nuclear heating in different layers of the UL calculated with a simple 4 layer limiter model.

	Nuclear heating [MW]					
	Box design		Plate design		Alternative plate design	
	HCPB	WCLL	HCPB	WCLL	HCPB	WCLL
PFW-1	1.99	2.57	2.00	2.56	2.00	2.60
PFW-2	1.04	1.34	1.02	1.32	1.02	1.32
PFW-3	1.06	1.38	0.88	1.11	0.87	1.09
SB	4.55	9.35	4.47	5.77	4.35	5.54
Sum	**8.64**	**14.6**	**8.37**	**10.8**	**8.24**	**10.5**

composition for the 4 layers of the limiter model can be found in Table 3.

Simulations for the three different configurations are performed using both the HCPB and the WCLL tritium breeding blanket (TBB). The results for the total values of nuclear heating in each of the layers are in Table 4 and radial profiles of nuclear heating in Fig. 9. It is found that the nuclear heating in the UL is higher for WCLL than for HCPB, and that while nuclear heating profile for different SB material compositions is similar in simulations with HCPB, the profile changes significantly with WCLL TBB.

Both the total values and radial profiles of nuclear heating are considered in the design of a next, more realistic model to determine the total amount of heat needed to be removed from each of the components and to determine appropriate spacing between cooling tubes, respectively.

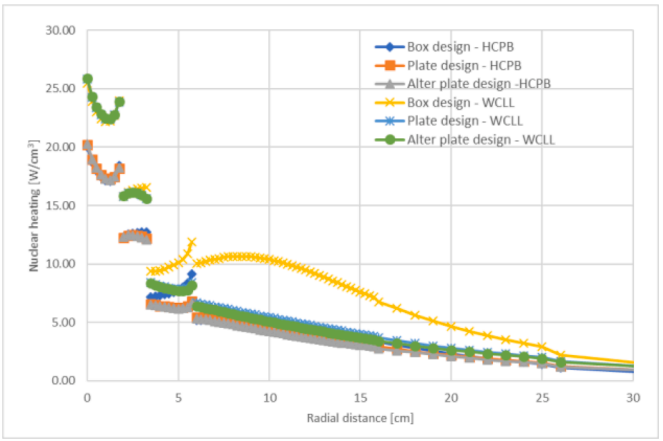

Fig. 9. Radial profile of nuclear heating for the analysed cases using the simple 4 layer limiter model.

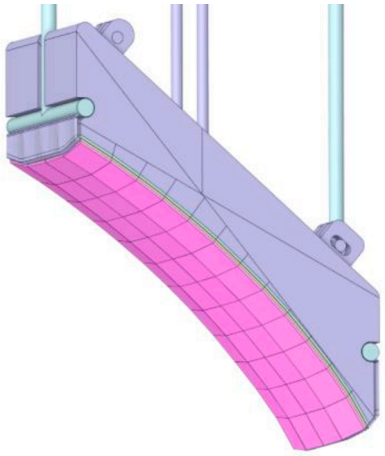

Fig. 10. CAD model of the UL geometry as used in neutronics simulations.

In the second stage of the neutronic analyses, the UL model follows the progress of the 3D UL design, as can be seen in Fig. 10. To maintain reasonable simplicity, the model still represents most of the components in homogenized form. However, the shape is significantly more realistic and PFW cooling pipes not covered by monoblocks are explicitly modelled with their related manifolds, while cooling pipes inside PFW monoblocks and SB are not. The PFW in this model is represented by 4 layers. The 4th layer is a representation of the PFW attachment system which is part of the 3rd layer in the simplistic model. The material composition of these layers can be seen in Table 5. For these analyses with a more detailed model, only the WCLL TBB model is conservatively used.

A more detailed representation of the geometry warrants more detailed 3D analysis of the nuclear heating profile inside the SB, which is

Table 5
Material composition (in%volume) of different layers in the detailed neutronics model of the upper limiter.

	Material composition
PFW-1 (20 mm)	W (100 %)
PFW-2 – layer with cooling pipes (17 mm)	Cu (11.70 %), CuCrZr (14.81 %), water (26.33 %, at 0.935 g/cm^3), W (47.17 %)
PFW-3 (3 mm)	W (100 %)
PFW attachment layer (23 mm)	Eurofer (21 %), void (79 %)
SB	Eurofer (92.85 %), water (5.28 % at 0.7 g/cm^3), Al_2O_3 (1.87 %)

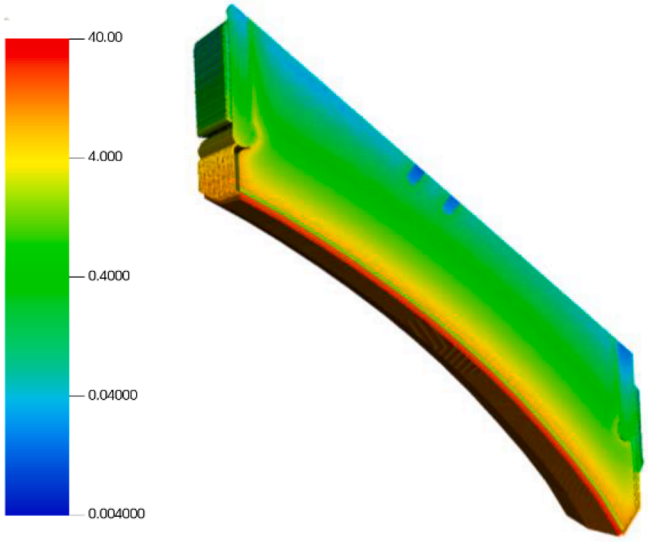

Fig. 11. Nuclear heating map (cut through the middle of the limiter) for a detailed model of the UL in W/cm^3.

Table 6
Total nuclear heating in each of the components for the detailed model of the UL.

Layer	Nuclear heating
PFW-1	2.35 MW
PFW-2	1.46 MW
PFW-3	0.376 MW
PFW attachment layer	0.171 MW
SB	5.18 MW
PFW cooling pipes (outside of PFW)	29.2 kW
PFW cooling liquid (outside of PFW)	34.4 kW
Sum	**9.60 MW**

then used as input to the thermal-hydraulic analyses described in §5.2. The 3D map of the nuclear heating is calculated using two Cartesian meshes, i.e. 2 mm × 4 mm × 4 mm for the front part and a 1 cm × 2 cm × 2 cm mesh for the values further from the PFWs, and can be seen in Fig. 11. The x-axis of these two meshes is perpendicular to the plane an the back of the SB and is thus relatively close to the radial direction for the entire limiter.

The total amount of nuclear heating deposited in each component is presented in Table 6. The values for "PFW cooling pipes (outside of PFW)" and "PFW cooling liquid (outside of PFW)" describe the amount of nuclear heating deposited in the part of the PFW cooling pipes outside the PFW and inside the manifolds servicing these pipes.

These results give a more refined picture of nuclear heating within the UL SB, highlighting that the total nuclear heating values in both detailed and simple models correspond reasonably well. This further supports and validates the approach followed in this study.

In addition to nuclear heating, neutron-induced damage of the material is also of interest for the design of the system. DPA rate in W and EUROFER is presented in Figs. 12 and 13, respectively. The peak values for the DPA rate in PFW and SB are 5.3 DPA/FPY and 8.4 DPA/FPY, respectively.

Another important aspect of the limiter integration is the impact of the UL on the neighbouring systems. Previous analyses [12] have shown that, due to the spatial constraints in the upper port region, the integration of systems there could be a challenge if HCPB TBB were used. In general, the UL is not problematic as it is effectively a shielding structure followed by another shielding structure (port plug in Fig. 8), but the large pipes of the TBB He cooling system represent a significant challenge for shielding the toroidal field coils on the inboard side. However,

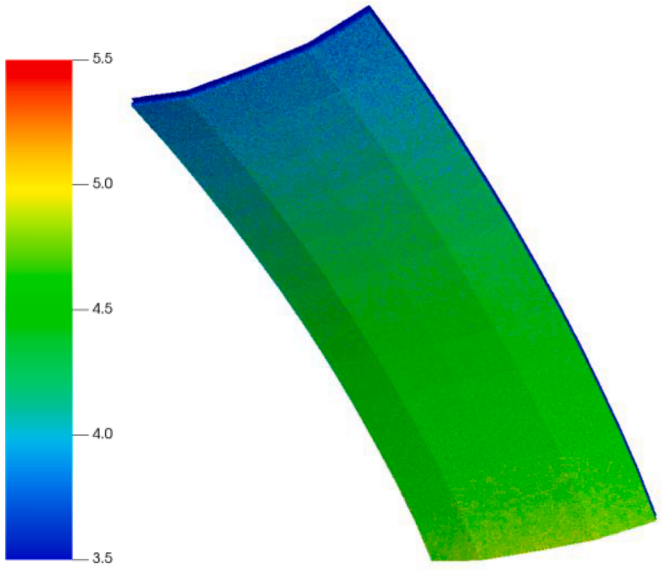

Fig. 12. DPA (in units of DPA/FPY) calculated in the W PFW of the UL.

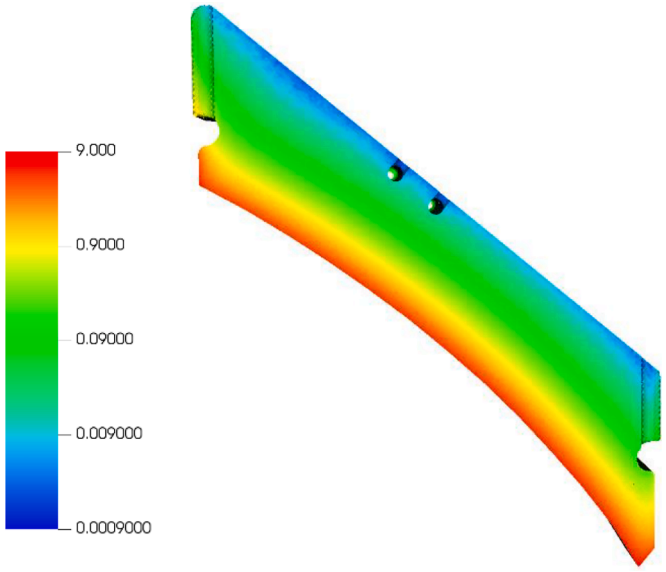

Fig. 13. DPA (in units of DPA/FPY) calculated in the EUROFER SB of the UL.

since our focus is on the case with WCLL TBB, this issue would be mitigated by the lower size of cooling pipes and by water flowing through these pipes, as opposed to He in HCPB. In this case, the maximum values of nuclear heating in the superconducting magnets are found to be 6 W/m^3, well below the DEMO limit for the peak value of nuclear heating in magnets of 50 W/m^3 [13]. The effect of the UL on the nuclear load in the vacuum vessel is also unproblematic, as the UL is located relatively far from the VV and has sufficient shielding performance.

5.2. Thermal hydraulics

In view of the complex PFW structure, which would require a computational grid fine enough to resolve all its components, the thermal-hydraulic assessment is carried out separately for the SB and the PFW, to exploit as much as possible all symmetries and periodicities. Therefore, they are reported separately in the following. All the models solves the Reynolds-Averaged Navier-Stokes equations with $k-\omega$ SST

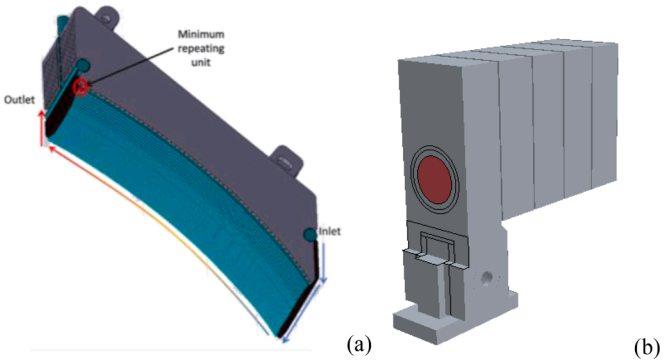

Fig. 14. (a) Location of the analysed (most disadvantaged) minimum repeating unit; (b) minimum repeating unit of the PFW, including five monoblocks and one support structure.

turbulence closure [14] and all -y^+ wall treatment, using the segregated approach; the commercial CFD software Star-CCM+ version 2021.2.1 (16.04.012) [15] is deployed.

5.2.1. PFW

As mentioned above, the PFW structure made of many W monoblocks does not allow the modelling of the entire system, which would become intractable from a computational point of view; therefore, the minimum repeating unit is analysed, as shown in Fig. 14.

To assess the design, the most conservative hypotheses are applied to this model, i.e. the largest possible value of volumetric neutronic power deposition is uniformly applied over the entire domain, and water is assumed to enter the domain at the average inlet-outlet temperature ($T_{ave} = 139\,^{\circ}C$). In addition to the volumetric heat load, a heat flux equal to 800 kW/m^2 is imposed on the plasma-facing surface, whereas on the contact surface between the support plug and the SB, the temperature computed from the SB simulation (see §5.2.2 below) is imposed to evaluate the heat transfer between the two regions. All the other surfaces are conservatively assumed as adiabatic: as the most penalized unit is analysed, it is safe to assume that nearby units radiate at lower temperatures.

The temperature and velocity distributions at the inlet of the domain are computed with a preliminary simulation using periodic BC, ensuring fully developed profiles for all the BCs (velocity, temperature, turbulent kinetic energy, and specific dissipation rate).

Before performing the thermal-hydraulic assessment of the minimum repeating unit, a purely hydraulic simulation (i.e. without any thermal load) is performed over the PFW cooling system domain, to assess the mass flow rate distribution among the 64 PFW units (32 in the symmetric domain). For this simulation, the overall mass flow rate of 81 kg/s is imposed as inlet BC, with the reference pressure (5 MPa) applied on the outlet surface.

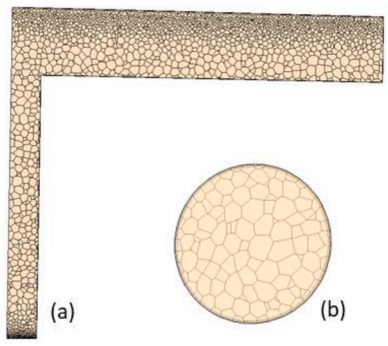

Fig. 15. Mesh used in the hydraulic PFW simulation; (a) detail of the manifold region; (b) detail of a pipe, showing the prism layer mesh.

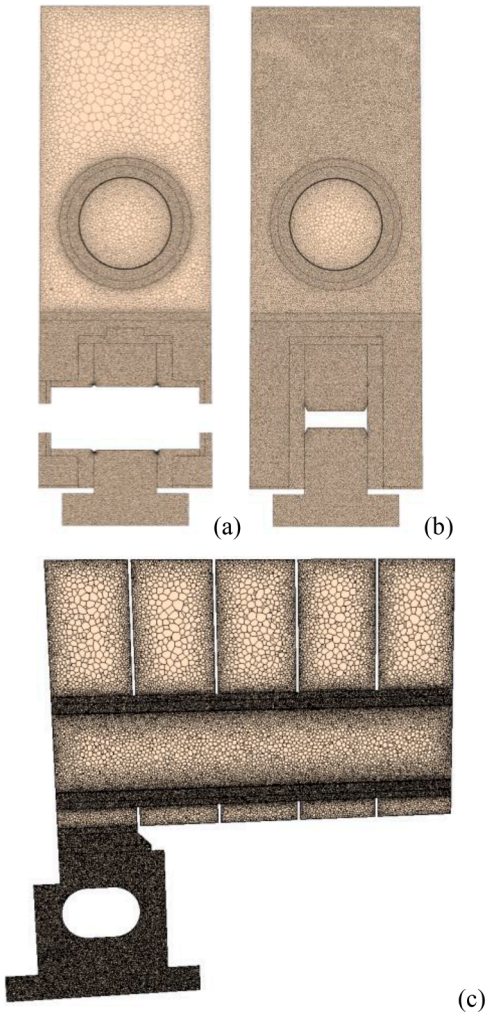

Fig. 16. Mesh used in the PFW simulation: (a) radial-poloidal plane cutting through the support structure pin hole; (b) showing the support structure plug; (c) poloidal-radial section.

The mesh used for the hydraulic simulation contains ~52 million cells, whereas that employed for the thermal-hydraulic assessment of the minimum repeating unit contains ~9 million cells, of which ~1.7 million in the fluid domain, ~1.6 million in the W monoblock, ~1.4 million in the CuCrZr heat sink pipe, ~1.1 million in the Cu interlayer pipe, and ~3 million in the support structure. Details of the two meshes are shown in Figs. 15 and 16, respectively.

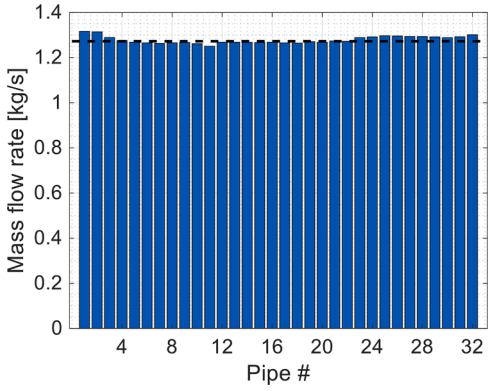

Fig. 17. Mass flow repartition in the PFW pipes; the black dashed line represents the average value.

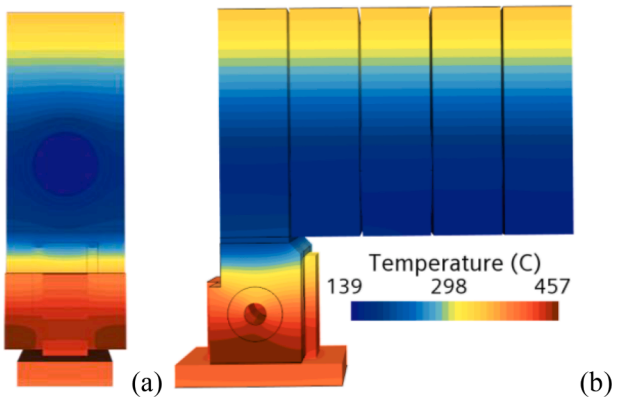

Fig. 18. Temperature distribution on the external surfaces of the PFW: (a) front view; (b) lateral view.

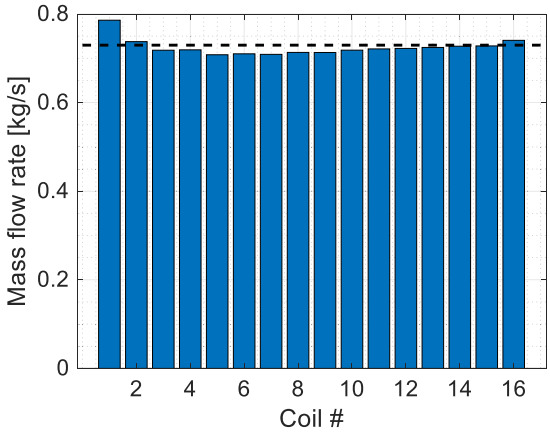

Fig. 20. Mass flow repartition in the SB cooling tubes; the black dashed line represents the average value.

The computed coolant mass flow distribution is rather uniform, as shown in Fig. 17 (where tubes are numbered as 1 → the closest to the inlet, 32 → the furthest from the inlet); the relative standard deviation is 1.3 %, with a maximum positive deviation of 2.9 % in pipe 1 (closest to the inlet) and a maximum negative deviation of −2.2 % in pipe 11, which is disadvantaged by the vortices forming when the coolant enters the manifold.

The total pressure drop across the PFW is calculated to be ~4.3 bar, of which 3 bar across the pipes and 1.3 bar in the manifolds; the maximum velocity in a PFW pipe is ~12 m/s, in line with the imposed value in Table 2.

Given this result, the minimum value of the mass flow rate (i.e. that corresponding to the most disadvantaged unit) is conservatively applied to the thermal-hydraulic assessment. Similarly, the largest local value of the volumetric power deposition computed by neutronic analyses (36 MW/m^3) is applied uniformly over the domain; in other words, this scenario simulates the minimum repeating unit which is simultaneously the one with the lowest mass flow rate *and* the largest heat load.

The temperature distribution on the external surfaces of the PFW minimum repeating unit is reported in Fig. 18. The EUROFER support structure reaches temperature below 300 °C in the region closer to the monoblock, thanks to the good W thermal conductivity and the relatively low water temperature. Such heat transfer is enhanced by the Cu interlayer embedded in the current PFW attachment [3] between the W monoblock and the support. An assessment with an additional Al_2O_3 layer between the interlayer and the support structure is also performed, proving that it is not sufficient to keep the temperature above 300 °C. A possible improvement to the existing support could be represented by the replacement of the Cu interlayer with a low thermal conductivity material, meanwhile studying new alternative attachment system layouts. Nevertheless, it should be noted that such temperature levels do not necessarily pose threats by themselves, until otherwise highlighted by dedicated thermal-mechanical assessments.

5.2.2. SB

In order to reduce as much as possible the computational cost, the Al_2O_3 layers separating the SB plates are not modelled, and the corresponding surfaces are considered adiabatic; this assumption is justified considering that (i) Al_2O_3 is a good thermal insulator (thus, making an adiabatic BC conservative), and (ii) the temperature is expected to be very similar across all the radial plate cross-sections, therefore minimizing the heat transfer. The lateral and PFW surfaces experience a radiative heat transfer, assuming a radiation temperature of 500 °C, whereas the VV-facing surfaces are exposed to a radiative heat transfer at 40 °C. As for the fluid BC, 23 kg/s of water at 285 °C enters the domain (see §4.2 above), while the reference pressure (15.5 MPa) is applied on the outlet surface. The computational mesh (Fig. 19) contains ~49 million cells, of which ~35 million in the fluid domain and ~14 million in the solid domain, reducing the domain to half due to toroidal symmetry. As volumetric heat load, the power deposition profile computed by neutronic analyses in §5.1 is applied.

The computed mass flow repartition among the 32 cooling tubes (16 in the symmetric domain) is reported in Fig. 20 (where the cooling tubes are numbered as 1 → the closest to the inlet, 16 → the furthest from the inlet); as shown, the mass flow distribution is acceptably close to

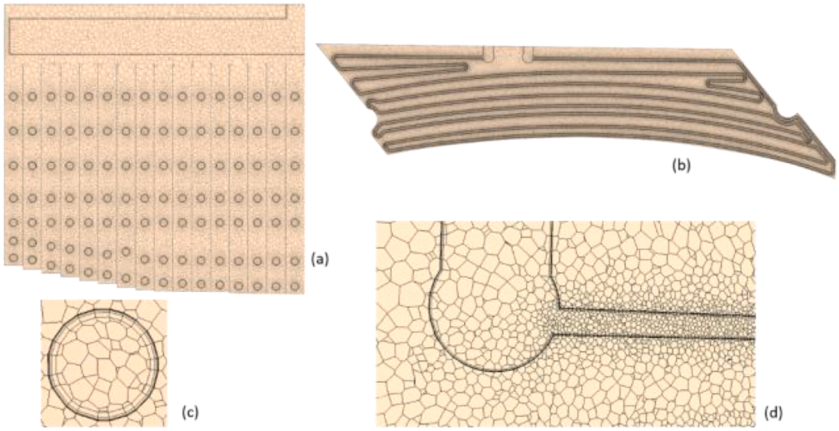

Fig. 19. Mesh used in the SB simulation: (a) cut across a poloidal-radial plane, including the manifold region; (b) cut on a toroidal-radial plane, across a plate; (c) detail of the mesh in a coil region, showing the prism layer meshing; (d) detail of the manifold region and coil inlet on a toroidal-radial plane.

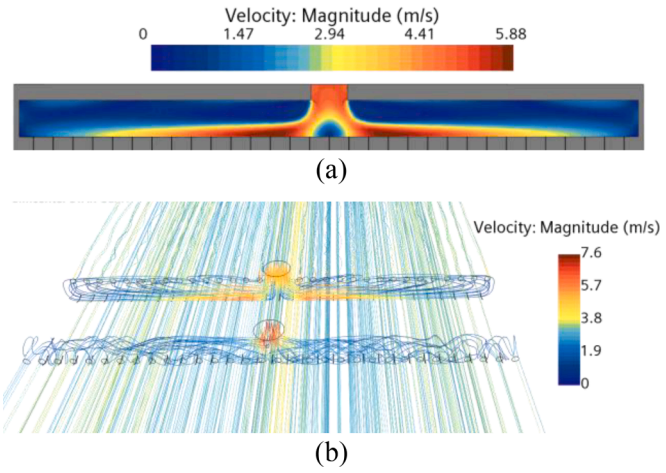

Fig. 21. Velocity field in the SB manifolds region: (a) speed map in the inlet manifold; (b) streamlines.

uniform, with a relative standard deviation of 2.6 %, a maximum positive deviation of 8.4 % in coil 1 (i.e. the most favourable, as it is the closest to the inlet), and a maximum negative deviation of −2.3 % in coil 5, which is disadvantaged by the vortices forming when the coolant enters the manifold as discussed in §5.2.1 for the PFW. This is shown in Fig. 21, where the velocity field in the inlet manifold region is reported.

The overall pressure drop is computed to be 1.06 bar across the SB, of which ~74 kPa are lost across the tubes and the remaining ~32 kPa in the inlet and outlet manifolds.

The temperature distribution across the SB is reported in Fig. 22 for a poloidal-radial cross section. This representation allows the verification of the hypothesis of adiabatic plate walls, as all the plate surfaces facing each other show similar temperature trends. The coolant distribution is adequate to keep the SB temperature well within the range 300–550 °C in most of the domain, except for the inlet manifold region where temperature reaches values below 300 °C, due to the low water inlet temperature and lower heat deposition value. This behaviour is however limited to the region around the inlet manifold and, in general, in the first part of the cooling tubes. If needed, a slight increase of the inlet temperature, e.g. to 295 °C (consistently with the WCLL Balance of Plant design [16]) would be sufficient to ensure the minimum temperature limit.

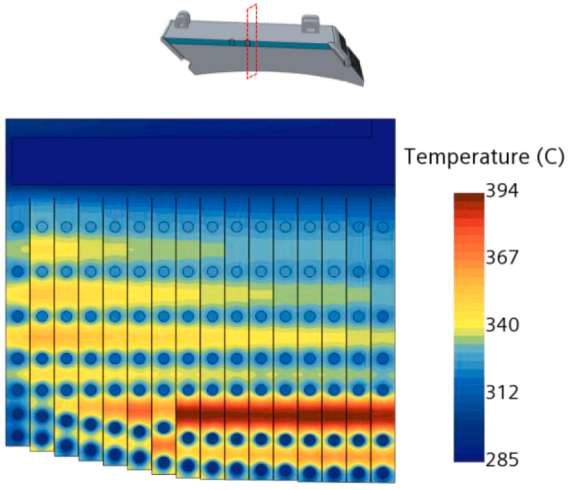

Fig. 22. Temperature distribution in a toroidal-radial cross section cutting the SB through the inlet manifold.

5.3. Electro-magnetism

5.3.1. FE model

The Finite Element (FE) model, developed to analyse the EM behaviour of the UL design under normal and off-normal operations, covers a span of 22.5° in the toroidal direction, encompassing a DEMO sector ranging toroidally from −11.25° to 11.25° The FE model is shown in Fig. 23 (top). This choice is preferred to modelling the entire 360° tokamak equipped with 8 ULs, as well as all the components within VV and cryostat, as observations during plasma disruptions indicate that the primary loads on in-vessel components result from net poloidal currents and current loops within the (radial-toroidal) cross-sections of these components. Consequently, any "relatively small" asymmetries in other sectors are likely to have minimal impact. This consideration, along with the need to limit the computational time needed for each analysis, supports the use of a single-sector approximation.

The approach to model one sector with symmetry condition has been frequently used to analyse in-vessel components (especially in the pre-conceptual phase) in tokamak facilities such as ITER [17,18], ASDEX upgrade [19], CFETR [20], K-DEMO [21] and DEMO itself [22,23].

The comprehensive methodology followed to implement the FE model has already been detailed in [22,23]. Nevertheless, for sake of clarity, key information regarding the model setup will be summarized in the following sections.

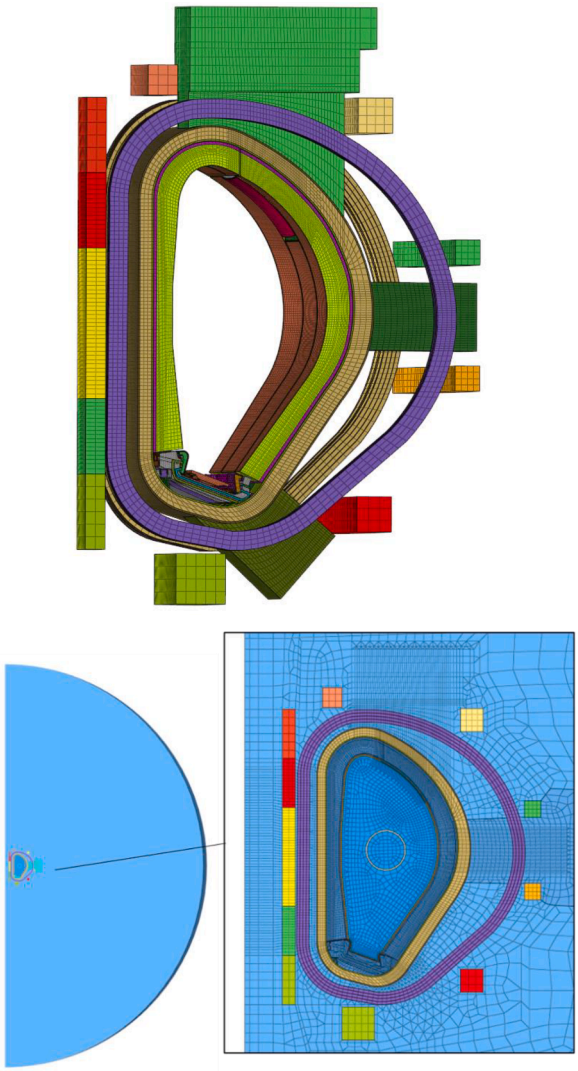

Fig. 23. Global model of the 22.5° DEMO sector.

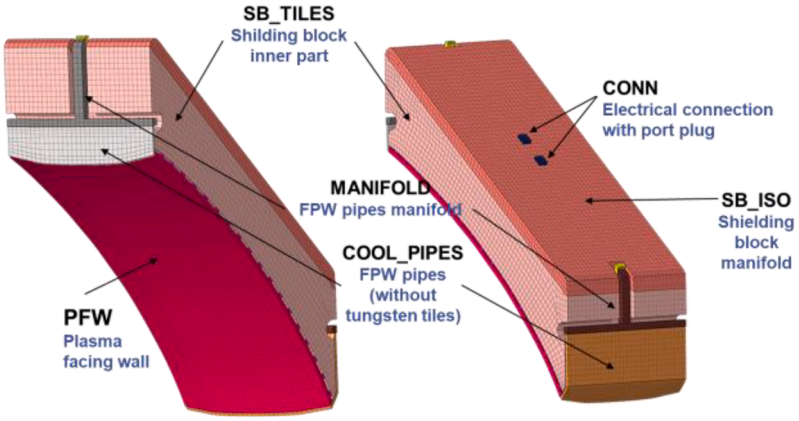

Fig. 24. Details of the UL geometry implemented into the FE model.

The FE model implements an enclosure that extends up to 120 m from the centre of the DEMO machine. This volume is visible in light blue in Fig. 23 (bottom). In addition to the UL, the FE model includes several components: the upper, equatorial, and lower ports and their respective port plugs, the five breeding blanket segments (two inboard and three outboard), the VV, the three divertors, the toroidal and poloidal field coil system (TFCs and PFs, respectively), and the plasma excitations. Conductive components and the coils system can be seen in Fig. 23.

5.3.2. UL FE model

As a common practice in preliminary analyses, most components are simplified in the FE model. Considering the design described in §4, the UL concept is divided into 6 sub-components, as represented in Fig. 24: the PFW, the SB tiles, the SB manifold, the cooling pipes (not covered by W monoblocks), the cooling pipe manifold, the electrical connection between PFW and SB, and the electrical connection with the port plug.

The homogenized EM material properties are established by considering the average temperature and material volume percentage within the integrated sub-component mesh. Isotropic properties are assigned to the SB and PFW manifolds, along with the SB-VV electrical connections. Meanwhile, orthotropic electrical properties are assigned to the PFW, cooling pipes, and SB tiles to prevent conduction along the toroidal (y-axis) direction. The conductive material, average temperature, and homogenized electrical resistivity for each sub-component are detailed in Table 7.

Additionally, an alternative model is developed considering the SB as a full box to quantitatively assess the reduction in eddy currents resulting from slicing the SB component. The sole variation in this model pertains to the SB_TILES material, adjusted to possess an isotropic electrical resistivity as outlined in Table 7 (refer to the comprehensive SB_TILES component details). Considering the small gap between the SB tiles (1 mm as reported in §4.2), no modifications in the electrical resistivity value are made with respect to the sliced SB. A comparative analysis of the results obtained from both the sliced and the full SB models is presented in §5.3.6.

5.3.3. Element type and boundary conditions

The modelling process involves using the SOLID236 element type [24] in ANSYS EMAG, a versatile element well-suited for addressing problems involving electromagnetic material property transitions at interfaces. This choice is made due to the predominant use of EUROFER [25], a ferromagnetic material, in the UL structural component.

The default key-options, all set to zero, are used for the vacuum region. The conductive region is modelled using the electromagnetic analysis option (KEYOPT(1)=1). This configuration establishes an electromagnetic element type, equipped with degrees of freedom for magnetic edge-flux (AZ) and electric potential (VOLT). Additionally, since the coils set is considered as a pure source term, KEYOPT(5) is set to 1 to suppress eddy currents.

Considering the underlying assumptions regarding the implemented sector, cyclic boundary conditions for AZ are imposed at the toroidal boundary nodes at -11.25° and $+11.25^\circ$ A parallel approach is followed for the VOLT degree of freedom, specifically targeting boundary nodes associated with conductive elements that exhibit toroidal continuity across the boundary planes. Since the developed DEMO sector is defined between two (half) TF coils, the last condition only affects the VV interface nodes. Indeed, no other conductive components are cut by the planes at $\pm 11.25^\circ$

As open boundary elements are not compatible with the edge-flux formulation, the AZ degree of freedom is set to 0 at the external spherical boundary surface of the enclosure. The enclosure's size (120 m radius) is chosen to optimize the mesh size while minimizing numerical solution errors due to that approximation. AZ is also set to 0 on nodes belonging to the axis, with one node on the axis left unconstrained to avoid constraining the toroidal flux to zero, as it is inconsistent with the physics of the problem.

5.3.4. Input loads

All sources of magnetic field, including plasma and CS, PF, and TF

Table 7
Equivalent electrical resistivity for the UL model, considering both full and sliced SB designs. Where not specified, electrical conduction is assumed to be zero.

Component name	Material	Temperature (°C)	ρ_x (μΩ m)	ρ_y (μΩ m)	ρ_z (μΩ m)
CONN (SB-VV electrical connection)	SS316	320	0.95	0.95	0.95
PFW_CONN (PFW-SB electrical connection)	EUROFER	320	0.85	–	0.85
PFW	CuCrZr	150	0.48	–	0.48
SB_ISO (SB manifold)	EUROFER	320	1.01	1.01	1.01
COOL_PIPES (cooling pipes)	CuCrZr	150	0.70	–	0.70
MANIFOLD (PFW manifold)	SS316	150	3.11	3.11	3.11
SB_TILES (Full box SB)	EUROFER	350	1.05	1.05	1.05
SB_TILES (Sliced SB)	EUROFER	350	1.05	–	1.05

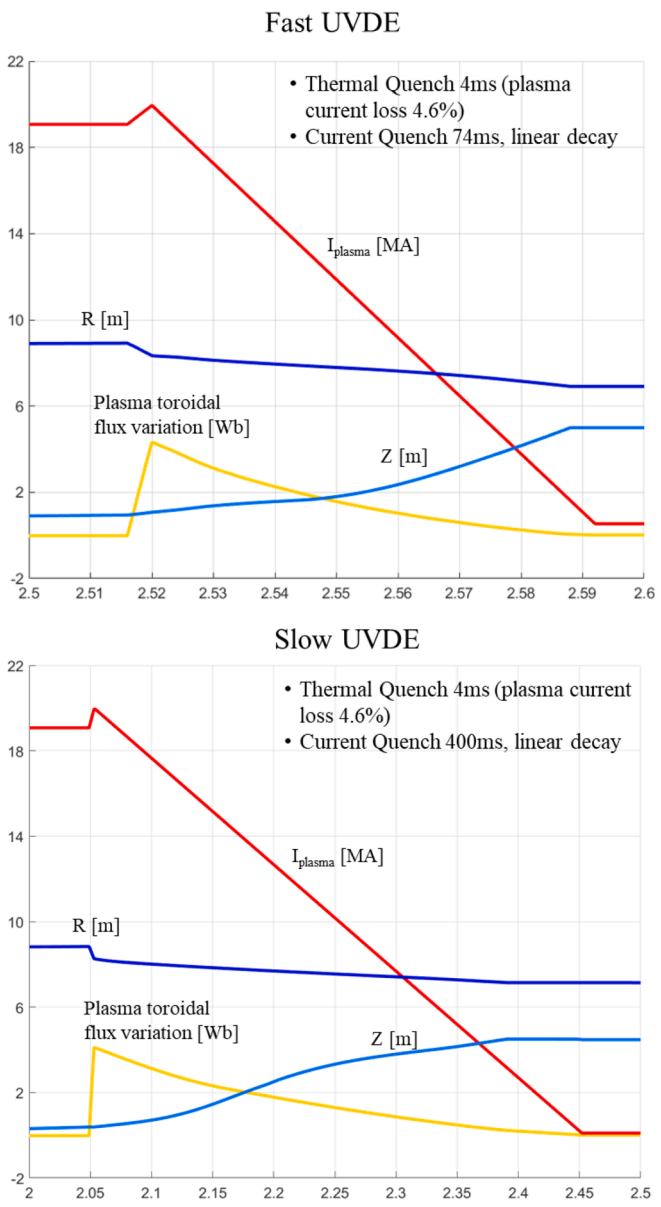

Fig. 25. Main parameters for the considered fast and slow UVDEs over time [s] (along the x-axis).

coils, are implemented for two EM scenarios: a fast UVDE and a slow UVDE.

Inputs for both plasma disruptions are derived from the CARMA0NL code [26]. They are characterized by a TQ of 4 ms and a linear decay of the plasma current during the CQ phase with characteristic times of 74 ms and 400 ms for the fast and slow events, respectively. Fig. 25 displays integral quantities of the plasma for both disruptions.

Plasma simulation strategy involves implementing the plasma using:

- An equivalent set of current filaments providing the same magnetic field as the plasma outside a coupling surface (Plasma Poloidal Field Variation, PFV) near the first walls (for the generation of the poloidal field).
- A fictitious toroidal solenoid (Plasma Toroidal Flux Variation, TFV) at the center of the plasma region fed by a current distribution that generates the necessary toroidal flux variation.

This approach allows simulating various electromagnetic scenarios without modifying the mesh. Fig. 26 provides an example of the current

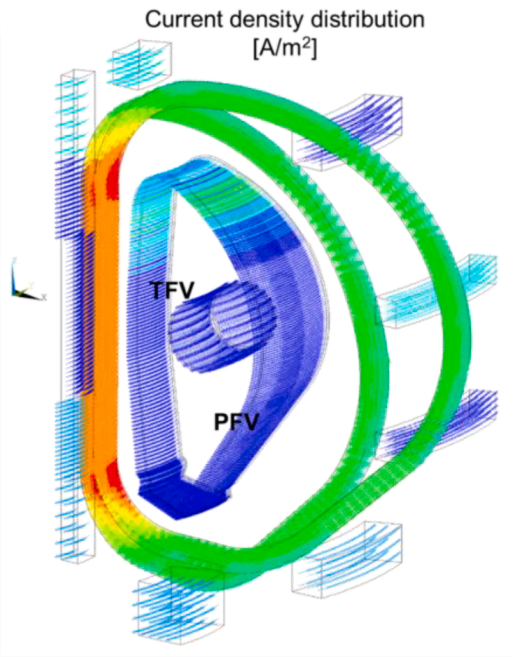

Fig. 26. Example of current distribution in the main source of magnetic field.

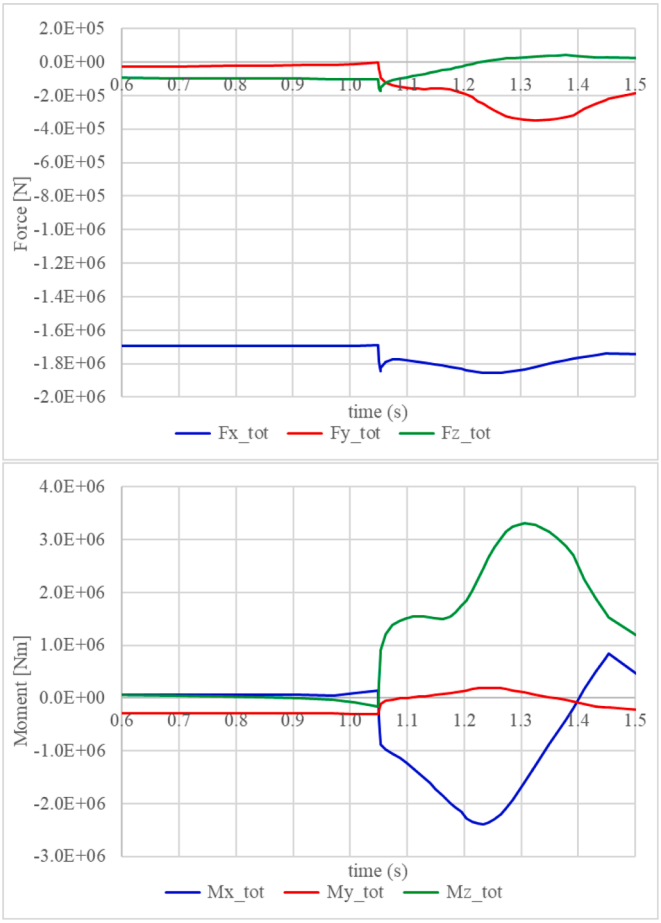

Fig. 27. Force and moment components exerted on the UL equipped with the full SB configuration in its local Csys.

distribution in the main source of the magnetic field.

5.3.5. EM results

The analyses performed in this study provide EM loads to support the DEMO UL design. Total force and moment values are reported below with respect to the UL local Cartesian coordinate system (Csys), which has the same orientation as the global coordinate system and is centered at the geometrical center of the UL.

5.3.6. Sliced vs full SB under slow UVDE

A set of analyses is performed to evaluate the reduction in EM loads due to the sliced configuration of the SB, compared to a full SB. Total force and moment acting on the entire UL system for the slow UVDE event are calculated and plotted in Figs. 27 and 28, respectively, for UL equipped with a full SB and a sliced SB. These calculations consider both the contribution of the ferromagnetic material (EUROFER), also present during normal operation, and the eddy currents induced during the transient.

During the TQ, the primary contribution to the EM loads is the radial force (F_x), which results from the gradient of the toroidal magnetic field and the interaction of the poloidal eddy currents generated by the variation of the plasma toroidal field and the magnetic field, mainly the toroidal component. For this component, there is no significant reduction between the two configurations under study because the generated eddy currents flow approximately in the same direction as the SB cutting planes (e.g., poloidally), exhibiting similar behaviour in both configurations (see also Fig. 29).

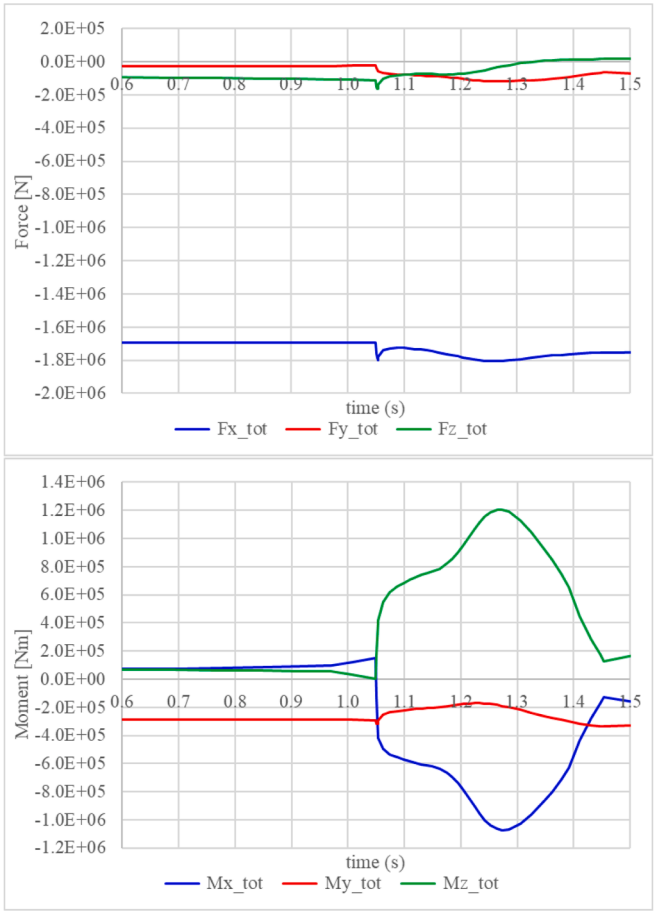

Fig. 28. Force and moment components exerted on the UL equipped with the sliced SB configuration in its local Csys.

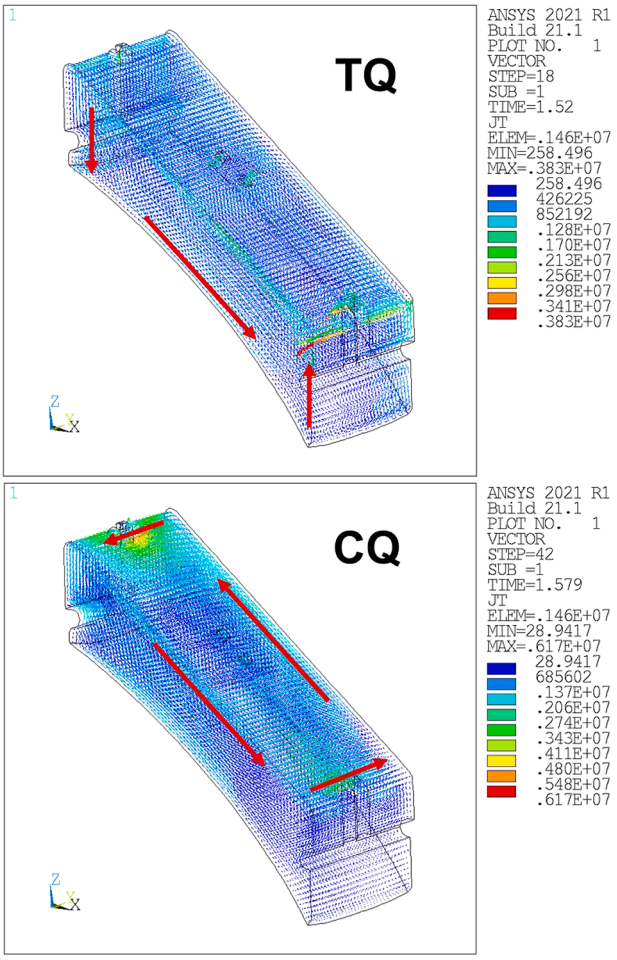

Fig. 29. Qualitative behavior of eddy currents in the UL equipped with a sliced SB during TQ and CQ.

However, during the CQ, the loads result from poloidal magnetic flux variation, which generated toroidal-radial current loops within the SB structures (see lower plot in Fig. 29). In the sliced SB configuration, the loops are cut due to the presence of electrical gaps between the slices, resulting in a 50–60 % reduction in moment.

Fig. 30 illustrates the peak values for each component of the EM loads (force and moment) calculated during TQ and CQ for the full and sliced SB designs.

5.3.7. Sliced SB under fast and slow UVDE

The second set of analyses compares the EM loads during fast and slow UVDEs. Since the variation of the plasma toroidal magnetic flux is the same for both plasma disruptions, no significant differences are found in the peak loads at the end of the TQ. However, due to its short characteristic current time, the UVDE fast event generates higher moments into the UL system as reported in Fig. 31.

5.3.8. Halo current contribution on the sliced SB during slow UVDE

As a final analysis, the contribution of the halo current during a slow UVDE is evaluated. The analysis is conducted by directly imposing the input from the CARMA0NL code into the first wall (in-vessel components plasma-facing walls) using the F command of ANSYS APDL. The calculated EM loads, attributable solely to halo current and excluding the ferromagnetic contribution, are reported in Fig. 32.

It is important to note that the behaviour of the halo current inside the UL structure can be strongly influenced by the electrical contacts with the port plug. In the considered case, the halo current, which enters

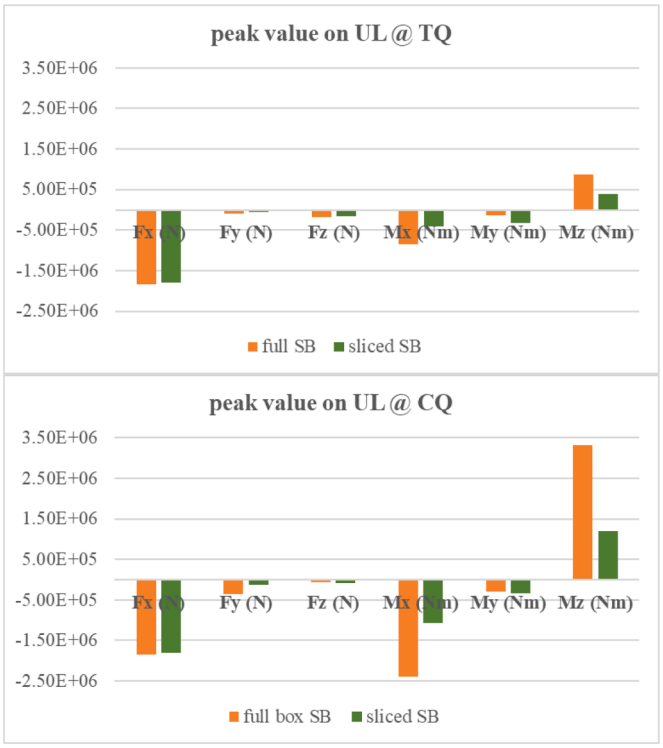

Fig. 30. Comparison of the EM peak values acting on both the UL equipped with a full and a sliced SB configuration during TQ and CQ. Loads are calculated with respect to the local Csys.

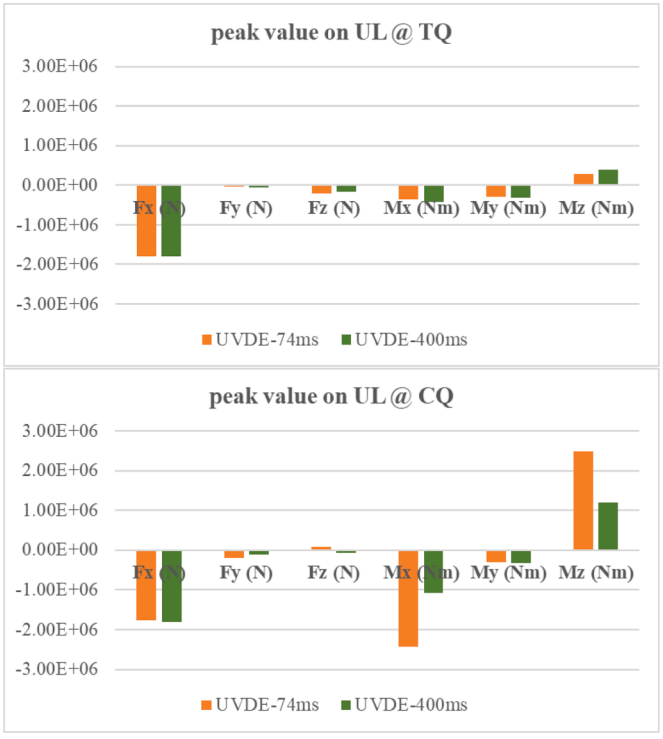

Fig. 31. EM effects on UL equipped with a sliced SB configuration under both fast and slow UVDEs. Loads are calculated with respect to the local Csys.

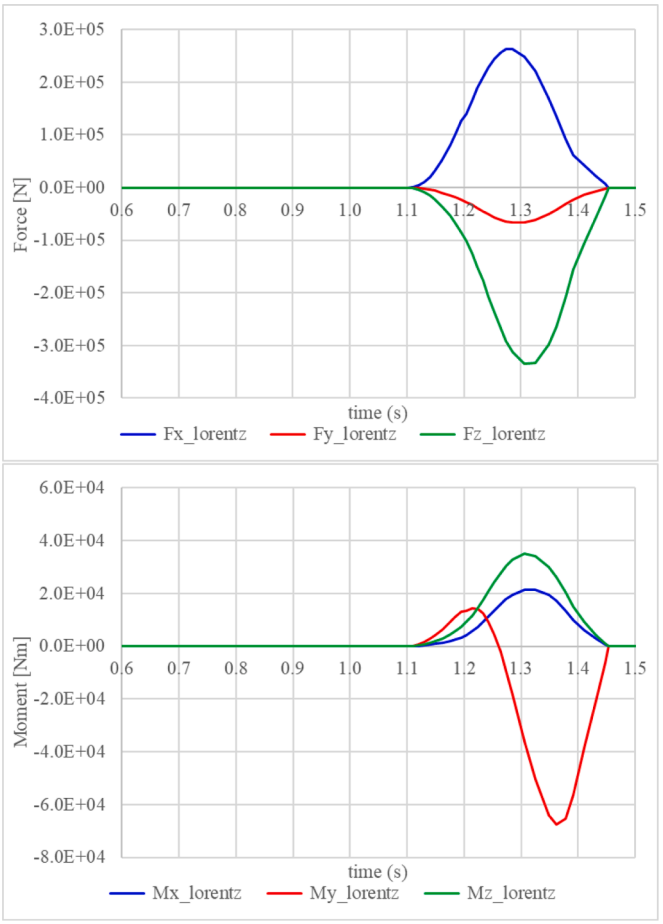

Fig. 32. Force and moment components resulting from the HC contribution to the UL equipped with the sliced SB configuration with respect to its local Csys.

the UL PFW and does not close within the same structure, flows directly into the PFW-SB electrical connections and, through the SB, reaches the electrical contacts with the port plug located in the central part of the SB manifold (see also Fig. 33). In this case, the cooling pipes are not heavily loaded. However, different configurations of the electrical contacts, such as having them only in the upper and lower parts of the SB manifolds, could result in the halo current flowing through the cooling pipes and manifolds as the shortest resistive path to reach the port plug. Such a case should be evaluated in the future to identify the most critical scenario for the structural assessment of the PFW-SB attachment system.

5.4. Structural assessment

To perform the structural assessment of the design, an FE model is developed, and the outcomes are fed to assessment rules to verify the structural integrity of the UL design. The modelling procedure and assumptions, outcomes and assessment results are explained in the following.

5.4.1. FE modelling

The FE model is developed using Ansys workbench 2022. The mesh is created in Hypermesh 2021 and imported in Ansys workbench environment. An overview of the mesh is shown in Fig. 34. Details about element type and numbers are reported in Table 8.

The model is developed with some simplifications, which includes the replacement of joints with kinematic constraints preserving the behaviour of the real system. In particular, the connections are conveniently defined to realistically simulate the effect of clearances between the internal components of each support. As far as the PFW-SB supports

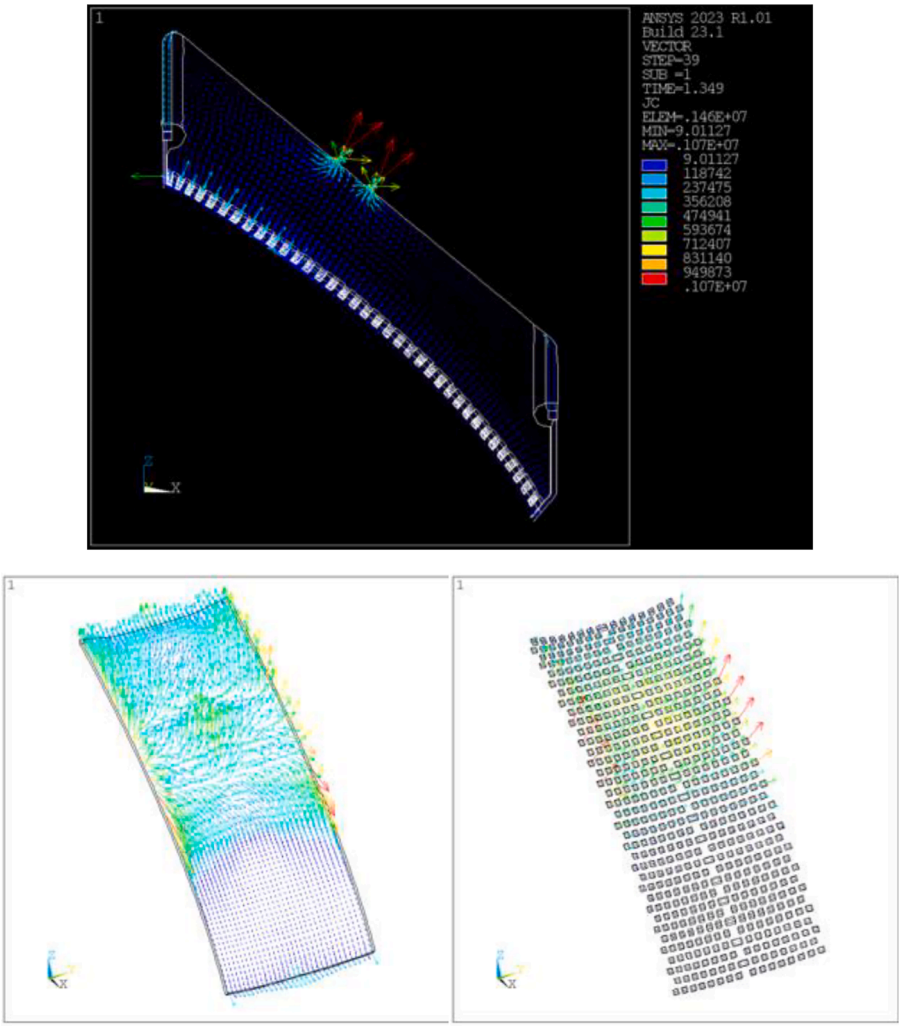

Fig. 33. Example of halo current distribution inside the whole UL system (top), the PFW (bottom left), and the PFW-SB attachment system (bottom right).

are concerned, free rotation around the pin axis and free translation along the pipe axis direction are defined between each monoblock and the related SB plate. Fig. 35 shows the comparison between the original CAD geometry and the simplified FE model of the PFW-SB supports, whereas Fig. 36 explains more details of these connections. A joint is defined between each pin (modelled with 1D elements) and the corresponding support plug (simulated with a 2D dummy element bonded to the SB plate). A clearance of 1 mm is considered between lug and plug, thus permitting translations and rotations.

As far as the SB-VV supports are concerned, the simple approximated geometry highlighted in green in Fig. 37 is used for modelling the VV side of the connections (Plugs), due to the lack of VV CAD model. The pins between the SB side (Lugs) and the VV side (Plugs) are modelled with 1D elements.

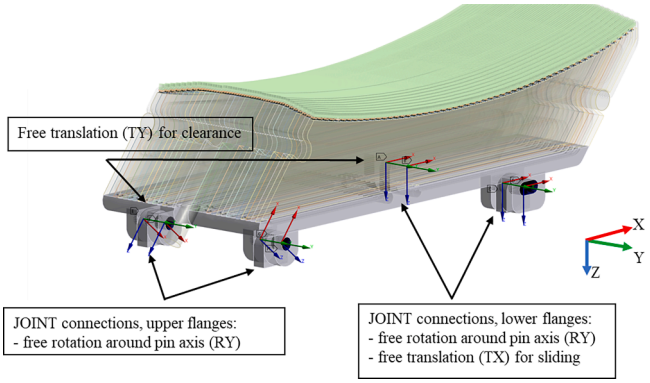

Fig. 38 shows the locations of the 8 joint connections defined with respect to local Csys for coupling the pin with the lugs. The degree of freedoms (DoFs) on the joint connections are defined as follows.

- On the four joints on the upper supports, rotations about the y-axis (RY in the local Csys) are only set free.

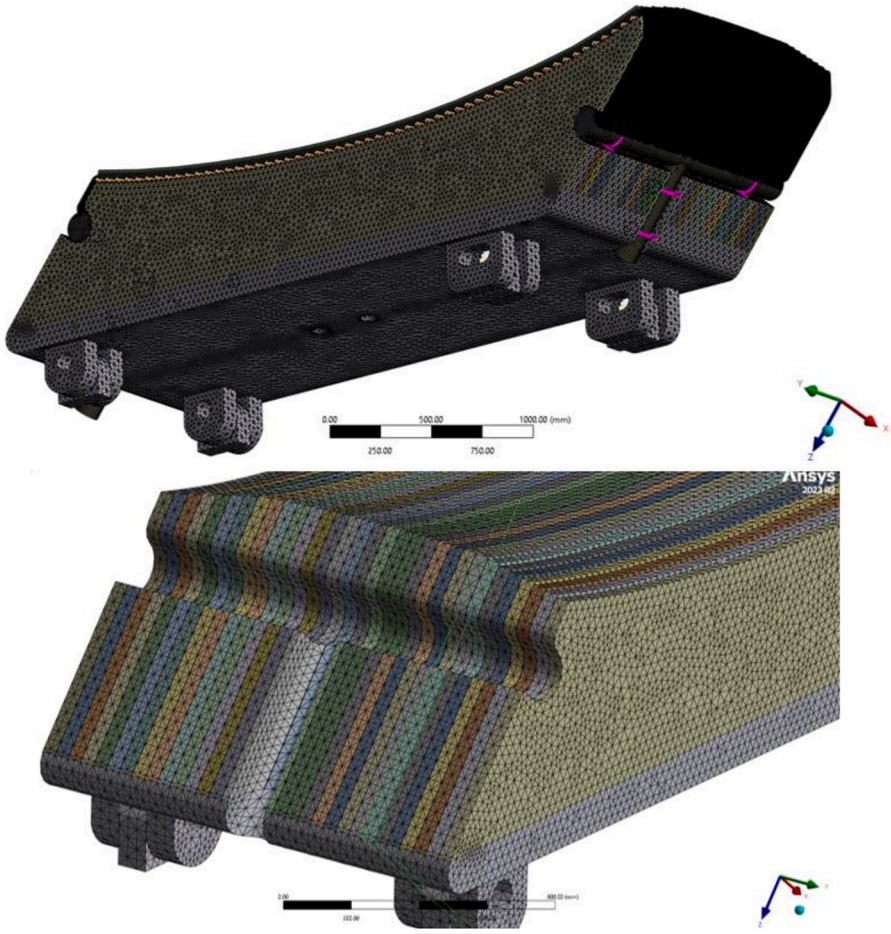

Fig. 34. Overview of developed mesh.

Table 8
Number of elements used in the structural FE mesh.

Element type	Element name	No°
4 Nodes Shell	Shell 118	527,744
3 Nodes Shell	Shell 118	198
8 Nodes Hexahedron	Solid 185	242,648
10 Nodes Tetrahedral	Solid 187	1,729,948
2 Nodes Beam	Beam 188	35,328

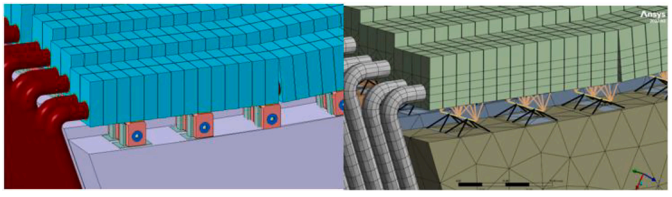

Fig. 35. PFW-SB supports, comparison between CAD geometry (left) and simplified FE model (right).

- On the four joints on the lower supports, in addition to RY rotations, translations along the x-axis (TX in the local Csys) are also set free to adequately simulate the sliding condition.
- On the four joints of the left-hand side supports (as indicated in Fig. 38), translations along the y-axis (TY in local Csys) are also set free to adequately simulate the 4-mm clearance between each lug and plug.

As illustrated in Figs. 39 and 40, the following bonded contacts are included in the model.

- Between SB back-plate and plates (Fig. 39).
- Between 2D dummy elements modelling the PFW-SB support plugs and their related SB plates (Fig. 40).

The DEMO VV port is assumed extremely stiff for the scope of the analysis. To simulate this condition in the FE model, the plug surfaces highlighted in green in Fig. 41 are fully constrained.

5.4.2. *Material properties*

Materials are assigned to the UL sub-systems according to §2. Materials' Elastic Modulus and coefficient of thermal expansion are reported in Tables 9 and 10, respectively.

5.4.3. *Loads*

The structure is studied under the following two load combination

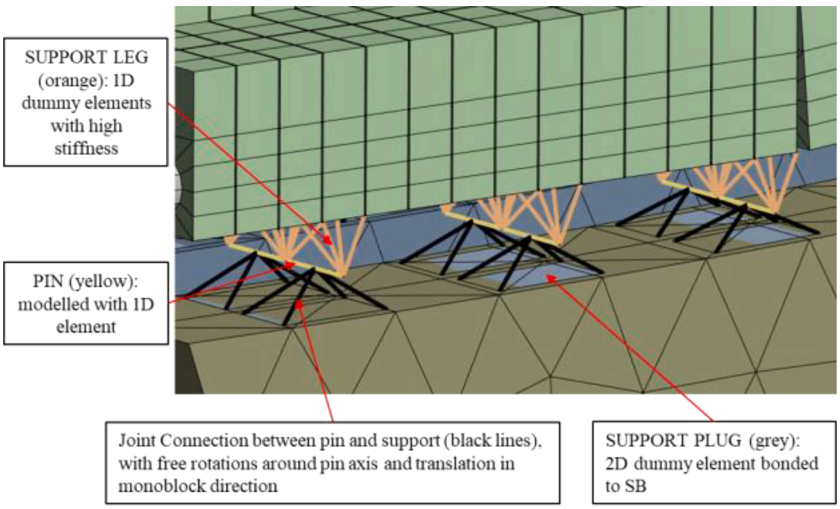

Fig. 36. Details of the simplified FE model of PFW-SB connection systems.

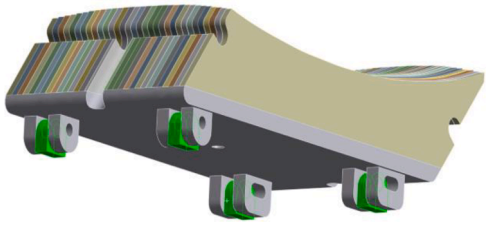

Fig. 37. Simplified geometry of VV support plugs (in green), introduced in the FE model to realistically constraint the UL.

cases: Load Combination 01 (LC#01), including Normal Operation + Fast UVDE; Load Combination 02 (LC#02), including Normal Operation + Slow UVDE + Halo-induced loads. The EM loads and the related events are described in §5.3. For every LC, Normal Operation encompasses Dead Weight, Cooling Pressure, and Temperature Distribution described in the following:

Dead weight: the load due to the Dead Weight of the UL itself is applied through the definition of standard Earth gravity: 9.8066 m/s^2 acceleration along the z-direction of the reference global Csys.

Cooling Pressure:

- Cooling Pressure on PFW manifolds and pipes: 5 MPa.
- Cooling Pressure on SB manifolds and channels: 15.5 MPa.
- Equivalent Axial Force, estimated by hand calculations, on each PFW manifold section: $F = 58{,}660$ N distributed on each cut end of PFW manifold feeding pipes to balance missing sections, directed along $Z+$ axis (global Csys).
- Equivalent Axial Force, estimated by hand calculations, on each SB manifold section: $F = 76{,}548$ N distributed on each cut end of SB manifold feeding pipes to balance missing sections, directed along $Z+$ axis (local Csys).

Temperature Distribution:

The steady-state temperature distribution coming from the thermal-hydraulic analyses in §5.2 is mapped across the structure.

The LCs are applied to the model by following a sequential approach, i.e. the single load cases are added step by step during subsequent time instants. Concerning the EM forces, several instants are studied. The sequence of loading for each LC is presented in Tables 11 and 12.

5.4.4. Sub-modelling

To investigate better the SB-VV supports, dedicated sub-modellings are developed for the different attachment points and assessed under reaction forces coming from the global model.

The design concept of the SB-VV attachment system in Fig. 6 is detailed in Fig. 42, where the different mechanical combinations are highlighted.

Whereas the upper SB-VV supports has a circular pin (Fig. 42-top), the lower SB-VV attachment concept foresees an oval shaped pin (Fig. 42-centre) to increase the contact area. In both the configurations, a 2 mm gap shown at the bottom of Fig. 42 is also added to avoid unnecessary interaction between lug and pin in the axial direction, thus reducing the consequent reaction forces on the pin. This makes nut and washer work as a stopper only once the relative displacement between pin and lug exceeds 2 mm. The design is made functional by iterations of analyses and modifications. The modelling and results of the last modification are presented in the following.

A fully constrained boundary condition is set on the bottom of the lower plate (grey plate) and the forces coming from the global model are applied on the upper plate. Frictional and bonding contacts are defined where needed as highlighted in Fig. 42. An enveloped load case which covers the maximum component of the loads coming from the global

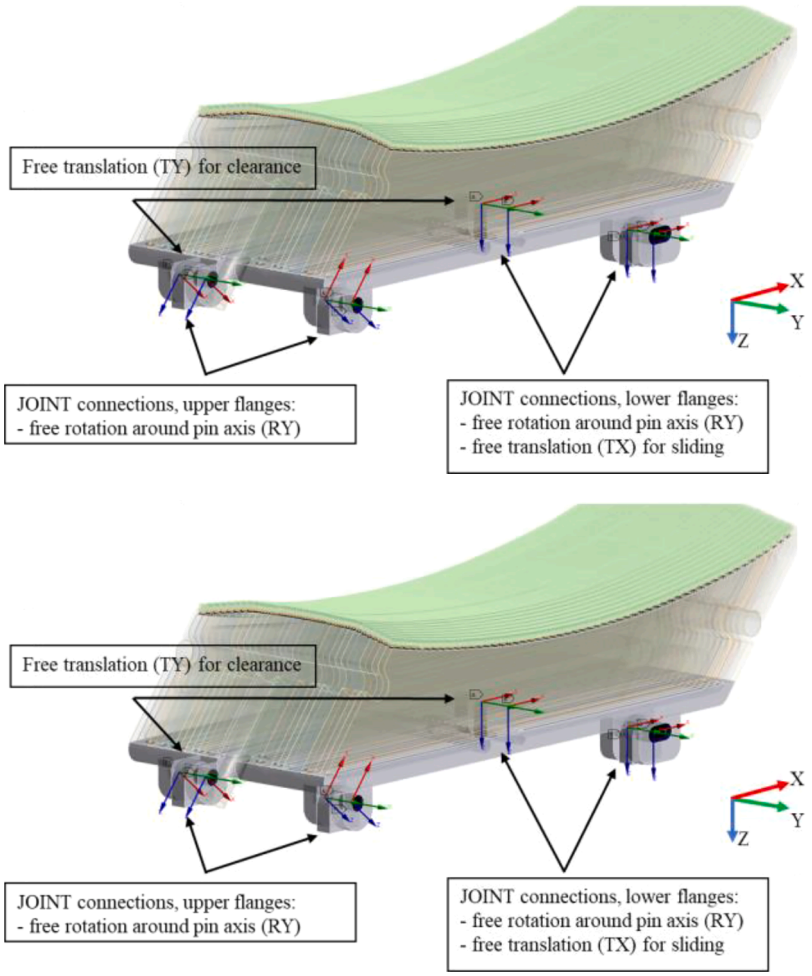

Fig. 38. FE model details of the SB-VV connections.

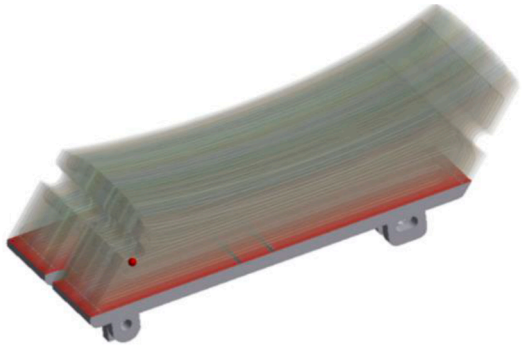

Fig. 39. SB back-plate (in grey) and SB plates (in transparency) bonding contacts.

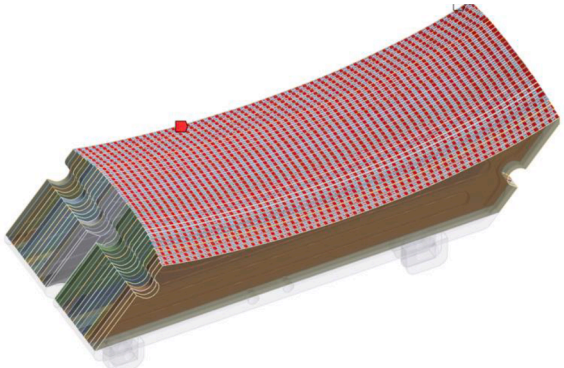

Fig. 40. PFW-SB supports bonding contacts.

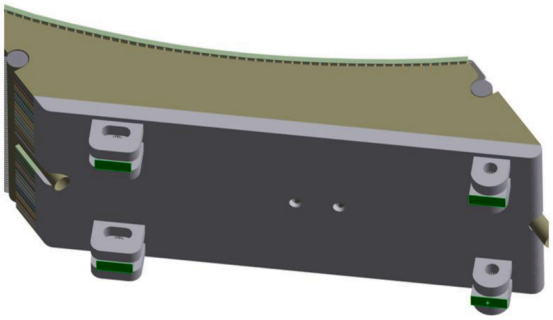

Fig. 41. VV plug fixed support (fully constrained) applied on the surfaces highlighted in green.

Table 9
Elastic Modulus of materials.

Temperature [°C]	Elastic Modulus [GPa]		
	EUROFER97	CuCrZr	W
0	219	130	396
25	217	129	396
50	215	128	396
100	212	126	395
200	207	122	394
300	202	116	392
400	196	110	389
500	190	103	386

Table 10
Thermal expansion of materials.

Temperature [°C]	Thermal expansion [10e-5/ °C]		
	EUROFER97	CuCrZr	W
0	1.01	1.68	0.44
25	1.03	1.68	0.44
50	1.05	1.68	0.44
100	1.07	1.69	0.44
200	1.12	1.71	0.44
300	1.16	1.76	0.44
400	1.19	1.83	0.45
500	1.22	1.91	0.45

Table 11
Sequence of loading – LC#01.

Steps	Load
1	Dead Weight (DW)
2	DW + Cooling Pressure (P)
3	DW + P + Temperature Distribution (T)
4	(DW + P + T) + VDE fast forces @ 0.407 [s]
5	(DW + P + T) + VDE fast forces @ 1.516 [s]
6	(DW + P + T) + VDE fast forces @ 1.520 [s]
7	(DW + P + T) + VDE fast forces @ 1.579 [s]
8	(DW + P + T) + VDE fast forces @ 1.584 [s]

Table 12
Sequence of loading – LC#02.

Steps	Load
1	Dead Weight (DW)
2	DW + Cooling Pressure (P)
3	DW + P + Temperature Distribution (T)
4	(DW + P + T) + VDE slow + Halo forces @1.053 [s]
5	(DW + P + T) + VDE slow + Halo forces @1.274 [s]
6	(DW + P + T) + VDE slow + Halo forces @1.285 [s]
7	(DW + P + T) + VDE slow + Halo forces @1.306 [s]
8	(DW + P + T) + VDE slow + Halo forces @1.454 [s]

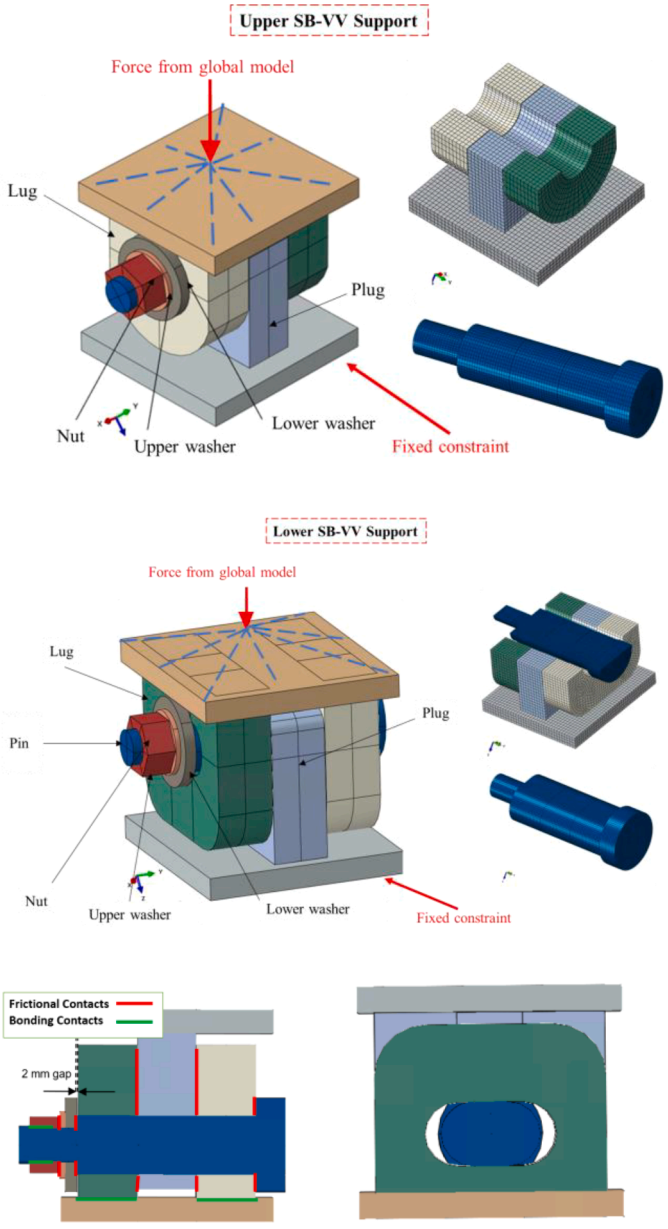

Fig. 42. Sub-modelling of upper SB-VV supports (top), lower SB-VV supports (centre), and cross-section of the lowers-VV support slotted hole (bottom).

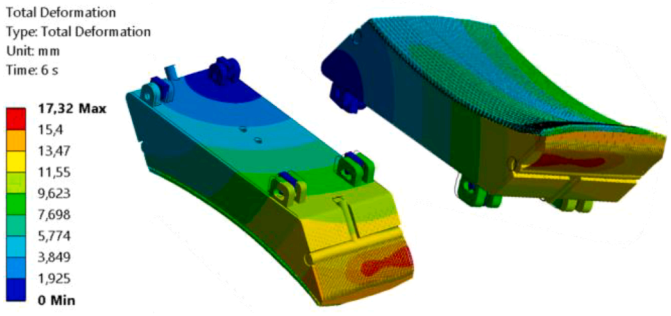

Fig. 43. LC#01: Displacement plot at step 6.

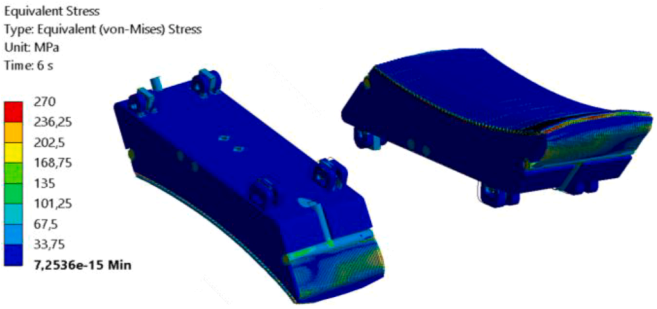

Fig. 44. LC#01: Stress plot at step 6.

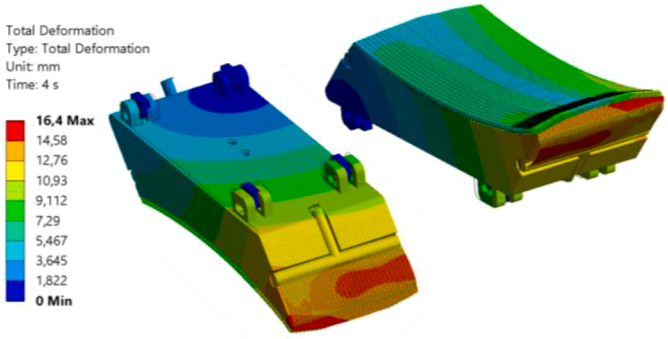

Fig. 45. LC#02: Displacement plot at step 4.

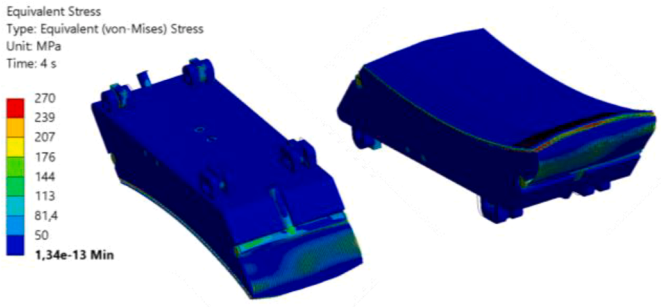

Fig. 46. LC#02: Stress plot at step 4.

model is applied on the upper plate using a reference point coupled to the top plate.

5.4.5. Results

The displacement and stress plots of LC#01 are presented in Figs. 43 and 44, respectively; the displacement and stress plots of LC#02 are instead presented in Figs. 45 and 46, respectively. Under both LCs, the major displacement is due to the thermal expansion (about 15 mm) with respect to the EM, which contributes to a max 2 mm displacement.

As far as the maximum displacement is concerned, it occurs at instant 6 under LC#01 and at instant 4 under LC#02. Concerning the stress

Table 13
Summary of assessment rules.

Symbol	Explanation
$\overline{P_m}$	Primary membrane stress
$\overline{P_L}$	Local primary membrane stress
$\overline{P_L + P_b}$	Local membrane plus bending stress
$S_m(\theta_m)$	Maximum allowable of the stress at the average temperature of θ_m
Assessment Type	**Rules for Level A Criteria**
P-type RB3251.112	$\overline{P_m} \leq S_m(\theta_m)$ $\overline{P_L + P_b} \leq 1.5 \times S_m(\theta_m)$
S-type Ratcheting RB3261.116	$Max(\overline{P_L + P_b}) + \overline{\Delta Q} \leq 3 \times S_m$

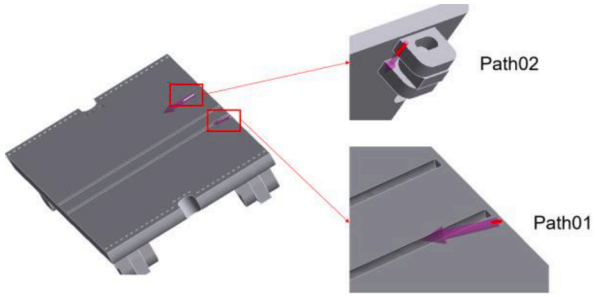

Fig. 48. Locations of Path01 and Path02.

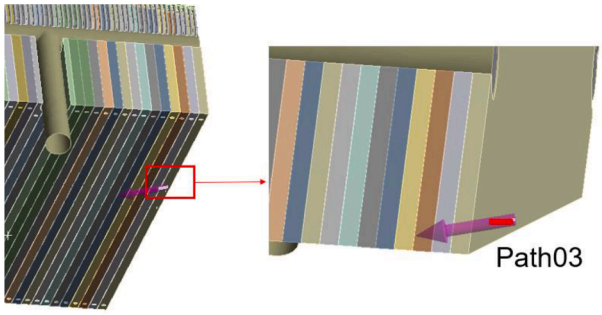

Fig. 49. Locations of Path03.

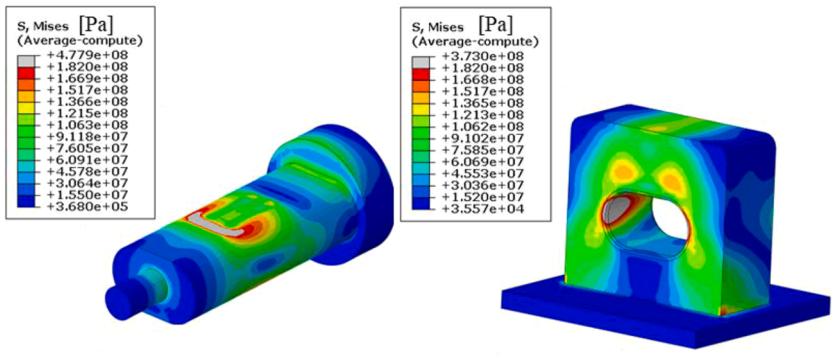

Fig. 47. Lower support stress plot resulting from the enveloped load case.

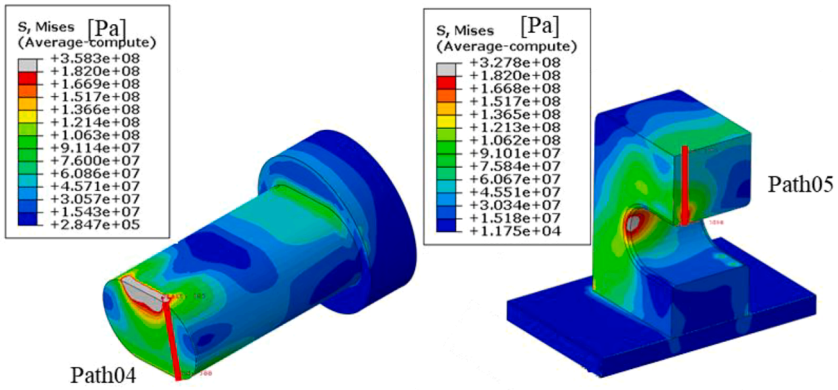

Fig. 50. Locations of Path04 and Path05.

Table 14
Summary of assessments under LC#01.

Location	P-type Margins	S-type Ratcheting Margins
Path01	2.98	4.7
	2.39	
Path02	4.46	7.6
	3.86	
Path03	7.17	>10
	6.88	

Table 15
Summary of assessments under LC#02.

Location	P-type Margins	S-type Ratcheting Margins
Path01	4.64	5.23
	2.6	
Path02	7.28	>10
	5.46	
Path03	>10	>10
	>10	

Table 16
Summary of assessments on SB-VV connection under Enveloped LC.

Location	P-type Margins
Path04	1.71
	1.24
Path05	1.91
	1.29

distribution, no criticality is observed in any of the LCs.

Fig. 47 presents the stress plot of SB-VV lower support resulting from the enveloped load case, which collects the most critical load components for the pin between the two analysed LCs. Although some local zones with high stress concentrations are observed, the structural integrity assessments are always satisfied, as will be discussed in the next section.

5.4.6. Structural integrity assessments

The structural assessment of the different models is performed under Level A criteria and following the procedure set by RCC-MR in [27]. The UL global model is assessed against P-type and S-type ratchetting verification rules, whose definition and summary is reported in Table 13. Table 13 also explains the basic stress components involved in this assessment.

Zones meriting being assessed are determined by screening the stress plots. The zones and paths used for assessment are highlighted in Figs. 48–50, whereas Tables 14–16 report the outcome of the assessments in terms of safety margins obtained by comparing the computed stress levels with the allowable limits (the Two P-type and S-type Margins are calculated based on the formulas reported in Table 13, respectively). As observed, no criticality is found.

6. Discussion

The assessment workflow of the integrated design of the UL supports the engineering choices behind the UL conceptual design. For each aspect, the following conclusions are highlighted.

- From the neutronics point of view, the integration of the UL has not been a major challenge due to its good shielding performance. The UL, equipped with a sliced SB, performs better with respect to the analysed systems, although all the configurations fulfil the shielding requirement towards neighbouring systems like VV and TFC, as a large part of the limiter is working as a neutron shield.
- The thermal-hydraulic assessment has proved that the EUROFER temperature lies within its operational window, with only small regions at temperatures below 300 °C; these should not be considered an issue unless otherwise proved by dedicated structural assessment, in particular on the PFW-SB attachment.
- The EM evaluation has proved that a sliced SB could reduce disruptive EM loads up to by 50–60 % during the CQ phase, which would justify the additional complexity of the design. Although halo current contribution is considered during slow UVDEs, it has not been found to be the most predominant contribution to the EM loads, under the more realistic scenario where the halo current is spread non-uniformly among all the IVCs. The position of the electrical contacts could play a role in shortening the halo current path across the structure, thus reducing their related EM loads.
- The structural assessment of the UL model has highlighted that the UL conceptual design is robust enough to safely withstand a combination of loads acting on the structure during both Normal Operation and accidental transients, like fast and slow UVDEs.

7. Conclusions

The UL conceptual engineering design is promising. Therefore, the UL design workflow and lessons learned are likely to be inherited by other sacrificial limiters. The PFW design development follows the up-to-date plasma physics assumptions, whereas technology R&D is ongoing within EUROfusion for investigating PFW solutions. A new R&D program is planned to start for investigating the technological feasibility of the SB layout. New PFW-SB fixation concepts will be investigated, as well as the effects of different electrical connection

locations. Integration issues have started to be addressed, supported by feedback from remote maintenance to drive realistic design handling.

CRediT authorship contribution statement

M.L. Richiusa: Conceptualization, Methodology, Software, Validation, Investigation, Visualization, Writing – review & editing. **A. Cardella:** Supervision. **A. Čufar:** Methodology, Software, Validation, Investigation, Visualization, Writing – review & editing. **A. Froio:** Methodology, Software, Validation, Investigation, Visualization, Writing – review & editing. **P. Haghdoust:** Methodology, Software, Validation, Investigation, Visualization, Writing – review & editing. **P. Ireland:** Supervision. **I. Maione:** Methodology, Software, Validation, Investigation, Visualization, Writing – review & editing. **I. Pagani:** Methodology, Software, Validation, Investigation, Visualization, Writing – review & editing. **G. Pautasso:** Supervision. **A. Martin Ramos:** Software. **G.A. Spagnuolo:** Project administration. **F. Vigano:** Methodology, Software, Validation, Investigation, Visualization, Writing – review & editing. **Z. Vizvary:** Supervision.

Declaration of competing interest

The authors declare that they have no known competing financial interests or personal relationships that could have appeared to influence the work reported in this paper.

Data availability

Data will be made available on request.

Acknowledgments

This work has been carried out within the framework of the EUROfusion Consortium, funded by the European Union via the Euratom Research and Training Programme (Grant Agreement No 101052200 — EUROfusion). Views and opinions expressed are however those of the author(s) only and do not necessarily reflect those of the European Union or the European Commission. Neither the European Union nor the European Commission can be held responsible for them.

This work has been (part-) funded by the EPSRC Energy Programme [grant number EP/W006839/1].

Computational resources were partly provided by HPC@POLITO, a project of Academic Computing within the Department of Control and Computer Engineering at the Politecnico di Torino (http://www.hpc.polito.it).

References

[1] F. Maviglia, et al., Integrated design strategy for EU-DEMO first wall protection from plasma transients, Fusion Eng. Des. 177 (113067) (2022).
[2] R. De Luca et al., "Pre-conceptual design of a PFC equipped with a W lattice armour for first wall limiters in the EU-DEMO fusion reactor," in *Fusion Eng. Des.*, 2023.
[3] J.H. You et al., "Divertor of the European DEMO: engineering and technologies for power exhaust," in *Fusion Eng. Des.*, 2022.
[4] M.L. Richiusa, et al., Advances in material phase change modelling approach for EU-DEMO limiter's plasma-facing components, Fusion Eng. Des. (2023).
[5] B.R. Munson, T.H. Okiishi, W.W. Huebsch, A.P. Rothmayer, Fluid Mechanics, John Wiley and Sons, 2013.
[6] A. Cardella, et al., The ITER port limiter system, in: Proc. 20th Symposium on Fusion Technology 43, 1998, pp. 75–92.
[7] F. Lucca, et al., EM DEMO model (Baseline 2017) including ferromagnetic effects of HCPB blanket modules-model with limiters, EUROfusion IDM (2019).
[8] C. Bachmann et al., "Overview over DEMO design integration challenges and their impact on component design concepts," 2018.
[9] Y. Wu, F.D.S. Team, CAD-based interface programs for fusion neutron transport simulation, Fusion Eng. Des. 84 (2009) 1987–1992.
[10] F. Brown, et al., Verification of MCNP5-1.60, Vols. LA-UR-10-05611, Los Alamos National Laboratory, 2010.
[11] JEFF 3.3, "https://www.oecd-nea.org/dbdata/jeff/jeff33/," [Online].
[12] A. Čufar, et al., Shielding concept and neutronic assessment of the European DEMO Upper port, in: Proceedings to 28th International Conference Nuclear Energy for New Europe, 2019.
[13] U. Fischer, et al., Neutronics requirements for a DEMO fusion power plant, Fusion Eng. Des. 9 (2015) 8–99.
[14] F.R. Menter, Two-equations eddy-viscosity turbulence models for engineering applications, AIAA J. 32 (8) (1994) 1598–1605.
[15] Siemens, "Star-CCM+ User's Manual," v14.06.
[16] L. Barucca, et al., Maturation of critical technologies for the DEMO balance of plant systems, Fusion Eng. Des. 179 (2022) 113096.
[17] P. Testoni, et al., F4E studies for the electromagnetic analysis of ITER components, Fusion Eng. Des. 89 (7–8) (2014) 1854–1858.
[18] T. Junquera, et al., Electromagnetic studies of effects produced by disruption events inside ITER European diagnostic port plugs, Fusion Eng. Des. 168 (2021) 112422.
[19] I. Zammuto, et al., The new ASDEX upgrade upper divertor for special alternative configurations: design and FEM calculations, Fusion Eng. Des. 171 (2021) 112468.
[20] X. Ma, et al., Electromagnetic force evaluation on the water cooled ceramic breeder blanket for CFETR, Fusion Eng. Des. 131 (2018) 21–28.
[21] S. Kwon, et al., Recent progress in the design of the K-DEMO divertor, Fusion Eng. Des. 159 (2020) 111770.
[22] I.A. Maione, et al., Electromagnetic analysis activities in support of the Breeding Blanket during the DEMO Pre-Conceptual Phase: methodology and main results, Fusion Eng. Des. 166 (2021) 112285.
[23] I.A. Maione, et al., Investigation of electromagnetic sub-modeling procedure for the breeding blanket system, J. Nucl. Eng. 4 (1) (2023) 165–176.
[24] ANSYS APDL Reference Manual. Available online: https://www.ansys.com/ (accessed on September 2023).
[25] K. Mergia, N. Boukos, Structural, thermal, electrical and magnetic properties of Eurofer 97 steel, J. Nucl. Mater. 373 (2008) 1–8.
[26] F. Villone, et al., Coupling of nonlinear axisymmetric plasma evolution with three-dimensional volumetric conductors, Plasma Phys. Control. Fusion 55 (2013) 095008.
[27] RCC-MRx, Design and Construction Rules For Mechanical Components of Nuclear installations: High temperature, Research and Fusion Reactors, AFCEN Edition, 2007.